The Astrophysical Journal, 754:67 (27pp), 2012 July 20 doi:10.1088/0004-637X/754/1/67

KINEMATIC SIGNATURES OF BULGES CORRELATE WITH BULGE MORPHOLOGIES AND SÉRSIC INDEX*

Maximilian H. Fabricius[1,2], Roberto P. Saglia[1], David B. Fisher[3], Niv Drory[4], Ralf Bender[1,2], and Ulrich Hopp[1,2]
[1] Max Planck Institute for Extraterrestrial Physics, Giessenbachstrasse, D-85748 Garching, Germany
[2] University Observatory Munich, Schienerstrasse 1, D-81679 Munich, Germany
[3] Laboratory of Millimeter Astronomy, University of Maryland, College Park, MD 29742, USA
[4] Instituto de Astronomia, Universidad Nacional Autonoma de Mexico (UNAM), A.P. 70-264, 04510 Mexico, D.F., Mexico
Received 2011 August 30; accepted 2012 April 20; published 2012 July 6

ABSTRACT

We use the Marcario Low Resolution Spectrograph at the Hobby–Eberly Telescope to study the kinematics of pseudobulges and classical bulges in the nearby universe. We present major axis rotational velocities, velocity dispersions, and h_3 and h_4 moments derived from high-resolution ($\sigma_{\rm inst} \approx 39$ km s^{-1}) spectra for 45 S0 to Sc galaxies; for 27 of the galaxies we also present minor axis data. We combine our kinematics with bulge-to-disk decompositions. We demonstrate for the first time that purely kinematic diagnostics of the bulge dichotomy agree systematically with those based on Sérsic index. Low Sérsic index bulges have both increased rotational support (higher v/σ values) and on average lower central velocity dispersions. Furthermore, we confirm that the same correlation also holds when visual morphologies are used to diagnose bulge type. The previously noted trend of photometrically flattened bulges to have shallower velocity dispersion profiles turns out to be significant and systematic if the Sérsic index is used to distinguish between pseudobulges and classical bulges. The anti-correlation between h_3 and v/σ observed in elliptical galaxies is also observed in intermediate-type galaxies, irrespective of bulge type. Finally, we present evidence for formerly undetected counter-rotation in the two systems NGC 3945 and NGC 4736.

Key words: galaxies: bulges – galaxies: formation – galaxies: general – galaxies: kinematics and dynamics – galaxies: photometry – galaxies: spiral – galaxies: structure

Online-only material: color figures, figure set

1. INTRODUCTION

There is ample observational evidence that bulges in early-type spiral galaxies come in different varieties. They are not all just like small elliptical galaxies which happen to live in the center of a spiral disk (Kormendy 1993; Kormendy & Kennicutt 2004).

While classical bulges seem to lie on photometric projections of the fundamental plane of elliptical galaxies (Fisher & Drory 2010) pseudobulges resemble disks more than they do little ellipticals. They are still photometrically distinct from the outer disk as they appear as a central brightening above the inward extrapolation of the outer exponential disk profile. However, as opposed to classical bulges, their Sérsic indices fall close to or below two (Fisher & Drory 2008). Other groups have shown that a large fraction of galaxies with boxy or peanut-shaped bulges do show signs of inner disks (Bureau & Freeman 1999; Chung & Bureau 2004; Kormendy & Barentine 2010). However, the phenomenon of inner disks is not limited to bulges that morphologically resemble disks as a whole (Scorza & Bender 1995; Emsellem et al. 2004; Falcón-Barroso et al. 2003, 2004; Sarzi et al. 2006; Falcón-Barroso et al. 2006; Comerón et al. 2010), although it seems ubiquitous in this class of objects.

Internal secular evolution is commonly seen as an important channel for the formation of central disk-like structures (Kormendy & Kennicutt 2004; Athanassoula 2005). In this picture, asymmetries such as spiral structure and bars support the angular momentum transfer of disk material and thereby the transport of gas into the inner bulge regions. In their recent study of bulges within the local 11 Mpc volume Fisher & Drory (2011) show that a majority of bulges in the local universe are pseudobulges. Their existence in large quantities in our local (low density) environment may seem to pose a problem for the understanding of the baryonic physics of galaxy formation (Kormendy et al. 2010) as, at first sight, it is not clear how central disks would survive the large quantity of low-redshift ($z < \approx 1$) mergers (Stewart et al. 2008) typical of Λ cold dark matter (ΛCDM) simulations (White & Rees 1978; White & Frenk 1991), but disk structures do not have to be destroyed in all mergers. Hopkins et al. (2008) show that the heating of the disks in a minor merging event is a nonlinear function of progenitor mass ratio once the satellite rigidity and the orbits are modeled properly. In addition to the impact parameters and the mass fraction, the baryonic gas content within the progenitors is an important parameter of the final result of a merging process (Hopkins et al. 2009; Stewart et al. 2009; Governato et al. 2009)—*wet mergers* are more likely to produce disks. Minor mergers may also create inner disk structures (Eliche-Moral et al. 2011) while increasing the Sérsic index only moderately (Eliche-Moral et al. 2006). Based on semi-analytical models for hierarchical growth which include prescriptions for the survival of disks, Fontanot et al. (2011) show that the existence of the majority of the galaxies with no significant bulge component in the local volume can be understood in the context of ΛCDM.

Kormendy & Kennicutt (2004) identify a number of criteria to differentiate between classical bulges and pseudobulges such as the bulge versus disk ellipticity, their location in the $v_{\rm max}/\sigma$ diagram, and bulge morphology. Fisher & Drory (2008, 2010) show that the Sérsic index of the bulge is successful in differentiating bulge types—pseudobulges have Sérsic indices that fall near or below $n = 2$, unlike classical bulges and elliptical galaxies which have higher Sérsic indices.

* This paper includes data taken at The McDonald Observatory of The University of Texas at Austin.

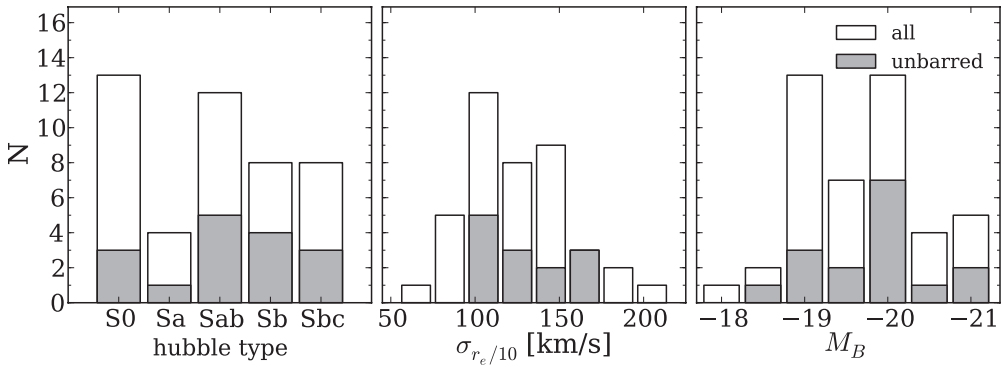

Figure 1. Distribution of Hubble types, central velocity dispersions, and total magnitudes in the sample.

The identification of the bulge morphology as well as the accurate derivation of photometric structural parameters heavily relies on high spatial resolution imaging. Recently, such data have become available for a large number of bulges. Adding sufficiently high-resolution spectroscopic data allows us to ask the question whether all morphologically disk-like bulges also show kinematic disk-like behavior, such as high v/σ values and/or flattening or drops in the σ profile? Also, whether differences seen in structural parameters such as Sérsic index are reflected in the kinematic structure as well?

In Section 2 we describe the sample selection and characteristics, in Section 3 we describe the long-slit observations, in Section 4 we give account on the derivation of *H*-band surface brightness profiles and their decomposition, as well as the details of the data reduction, especially the removal of emission features, and finally the kinematic extraction. Our results are presented in Section 5, in Section 6 we discuss correlations between kinematic parameters and morphological parameters and indications for an increased rotational support of pseudobulges. We finally discuss and summarize our findings in Section 7.

2. SAMPLE

As we aim to study the kinematics of bulges, our sample consists of 45 galaxies spanning the full range of Hubble types that do contain bulges: S0 to Sbc. Further, roughly two-thirds of our galaxies are barred, a similar fraction to the total fraction of bars observed in the local universe (see Figure 1). Table 1 lists the objects in our sample. For signal-to-noise (S/N) reasons we are biased toward high-luminosity objects. Absolute *B*-band magnitudes span the range from $M_B = -17.3$ to $M_B = -21.3$. Central velocity dispersions lie between 60 km s^{-1} and 220 km s^{-1}. We select our targets to be located close enough in distance to properly resolve the bulge regions in typical seeing conditions. With the exception of NGC 2964 and NGC 4030, all galaxies have bulge radii larger than 5 arcsec and are typically located at distances closer than 25 Mpc. Only NGC 4030, NGC 4260, and NGC 4772 are located at significantly larger distances of 29.3 Mpc, 48.4 Mpc, and 40.9 Mpc, respectively. The bulge radii of 7.3 arcsec and 23.5 arcsec of the latter two leave us confident that we are able to nevertheless sufficiently resolve their bulges. NGC 2964 and NGC 4030 have bulge radii of 3.1 arcsec and 3.0 arcsec, and are excluded from all structural analysis concerning the bulges, we restrict ourselves to presenting their kinematic data.

In order to break the known degeneracy between the bulge effective radius and Sérsic index in one-dimensional surface brightness decompositions (Graham & Colless 1997) we require all our targets to have *Hubble Space Telescope* (*HST*) imaging in F160W, *I*, or *R* band. Most of the objects are found in Fisher & Drory (2008) and/or Fisher & Drory (2010) and have extensive *HST* and ground-based multiwavelength coverage. To allow for a visual inspection and morphological classification of the bulge region we select objects which have close-to *V*-band *HST* images of their bulge region (see Section 4.3) available from the archive and we do not observe edge-on or close-to edge-on objects ($i > 70°$). Four objects in our sample do have a larger inclination. NGC 1023 and NGC 4371 are S0 types and contain very little dust and allow an undisturbed view into the bulge region. The situation is different for NGC 3593 and NGC 7331, where the inclination and—in the case of NGC 3593—the absence of an optical *HST* image inhibits a morphological classification. We present the kinematic data for those objects but refrain from classifying them as classical or pseudobulges.

3. OBSERVATIONS

We obtain major axis spectra for all and minor axis spectra for about half of the galaxies in our sample. In some cases the observed position angle is not identical to the one published in Hyperleda[5] (Paturel et al. 2003). Also, in a few cases the *minor axis* position angle is not orthogonal to the major axis position angle. We label observations accordingly in Table 2.

Observations were carried out in service mode during the period from 2005 April to 2010 April (see Table 2) at the Hobby–Eberly Telescope (HET; Ramsey et al. 1998) at McDonald Observatory. We use the Marcario Low Resolution Spectrograph (LRS; Hill et al. 1998) with a 1″ wide and 3.5′ long slit, the E2 phase volume holographic GRISM, and a Ford Aerospace 3072 × 1024 15 μm pixel (usable range 2750 × 900 pixel) CCD detector yielding a spatial scale of 0.235 arcsec pixel^{-1}. The spectra cover the wavelength range from 4790 Å to 5850 Å with 0.38 Å pixel^{-1} and a median instrumental resolution of $\sigma_{\rm inst} = 39.3$ km s^{-1} (as measured on the 5577 Å night-sky line). The seeing varies from 1.2″ to 4″ with a median value of 2.2″. Integration times vary from 1.800 s to 3.800 s and on-object exposures are typically split into two for cosmic rejection. For large galaxies where the DSS image of the galaxy exceeds the slit length, we obtain separate exposures of empty sky with an exposure time of 420 s at the end of the science observation. In order to avoid an azimuth move of the telescope, the sky exposures are typically obtained one hour in right ascension after the object but at similar declination.

[5] http://leda.univ-lyon1.fr

Table 1
Galaxy Sample

Galaxy	htype	D (Mpc)	src_D	M_B (mag)	i (°)
(1)	(2)	(3)	(4)	(5)	(6)
NGC 1023	.LBT-..	11.5	2	−20.0	77
NGC 2460	.SAS1..	23.6	1	−19.1	44
NGC 2681	PSXT0..	17.2	2	−20.1	0
NGC 2775	.SAR2..	14.4	1	−19.8	41
NGC 2841	.SAR3*.	9.0	1	−19.7	68
NGC 2859	RLBR+..	25.4	1	−20.2	33
NGC 2880	.LB.-..	21.9	2	−19.2	68
NGC 2964	.SXR4*.	19.9	1	−19.1	58
NGC 3031	.SAS2..	3.9	2	−20.1	59
NGC 3166	.SXT0..	22.0	1	−20.4	56
NGC 3245	.LAR0*.	20.9	2	−19.9	67
NGC 3351	.SBR3..	8.6	1	−19.1	42
NGC 3368	.SXT2..	8.6	1	−19.6	55
NGC 3384	.LBS-*.	8.6	1	−18.8	62[a]
NGC 3521	.SXT4..	8.1	1	−19.7	42
NGC 3593	.SAS0*.	8.8	1	−17.9	75
NGC 3627	.SXS3..	12.6	4	−20.9	57
NGC 3675	.SAS3..	10.7	1	−19.1	60
NGC 3898	.SAS2..	21.9	1	−20.1	57
NGC 3945	RLBT+..	19.0	1	−19.6	63
NGC 3953	.SBR4..	13.2	1	−19.8	62
NGC 3992	.SBT4..	22.9	5	−21.2	47
NGC 4030	.SAS4..	29.3	6	−21.1	40
NGC 4203	.LX.-*.	15.1	2	−19.1	27
NGC 4260	.SBS1..	48.4	7	−20.7	70
NGC 4274	RSBR2..	12.5	1	−19.1	66
NGC 4314	.SBT1..	12.5	1	−19.1	16
NGC 4371	.LBR+..	14.3	1	−19.0	79
NGC 4379	.L..-P*	15.9	8	−18.4	42
NGC 4394	RSBR3..	14.3	1	−19.0	20
NGC 4448	.SBR2..	12.5	1	−18.5	52
NGC 4501	.SAT3..	14.3	1	−20.4	61
NGC 4536	.SXT4..	12.2	9	−19.3	59
NGC 4569	.SXT2..	14.3	1	−20.5	66
NGC 4698	.SAS2..	14.3	1	−19.3	51
NGC 4736	RSAR2..	4.2	1	−19.1	35
NGC 4772	.SAS1..	40.9	5	−21.1	68
NGC 4826	RSAT2..	7.5	2	−20.0	60
NGC 5055	.SAT4..	7.8	1	−20.2	56
NGC 5248	.SXT4..	14.8	1	−19.9	56
NGC 5566	.SBR2..	20.1	5	−20.1	61
NGC 7177	.SXR3..	19.8	1	−19.5	42
NGC 7217	RSAR2..	16.6	1	−19.8	36
NGC 7331	.SAS3..	15.5	1	−20.8	75
NGC 7743	RLBS+..	19.2	10	−19.0	40

Notes. (1) Galaxy name. (2) Hubble type (RC3). (3) Distance. (4) Source for distance: 1 = Tully (1994) 2 = Tonry et al. (2001) 3 = de Vaucouleurs et al. (1991) 4 = Saha et al. (2006) 5 = Tully et al. (2009) 6 = Springob et al. (2009) 7 = Ekholm et al. (2000) 8 = Blakeslee et al. (2009) 9 = Riess et al. (2009) 10 = Jensen et al. (2003). (5) Total B-band magnitude (Hyperleda). (6) Inclination (Hyperleda).
[a] No value in Hyperleda, from P. Erwin (2011, private communication).

Furthermore we observe a collection of kinematic template stars (G and K giants, see Table 3, metallicity: [Fe/H] = −0.35 – 0.46) at the beginning and spectroscopic standards throughout the duration of this campaign. The stars are wiggled and trailed along the slit such that a spectrum is recorded at each position where the star crosses the slit. This is used to map out the anamorphic distortion of the spectrograph.

Table 2
List of Observations

Galaxy	Axis	Date	Seeing (″)	Exp. Time (s)	Angle (°)	Sky
(1)	(2)	(3)	(4)	(5)	(6)	(7)
NGC 1023	MJ	2009 Oct 24	1.9	2400	87	yes
NGC 1023	MN	2009 Oct 23	2.2	2400	177	yes
NGC 2460	MJ	2005 Nov 8	2.0	1800	30	no
NGC 2460	MN	2005 Nov 8	2.0	1800	120	no
NGC 2681	MJ	2007 Oct 21	2.0	2700	114	yes
NGC 2775	MJ	2008 Mar 5	2.6	2700	156	no
NGC 2775	MN	2008 Dec 24	3.4	2400	66	no
NGC 2841	MJ	2007 Nov 8	1.6	1800	152	no
NGC 2841	MN[a]	2008 Dec 23	3.2	2280	58	no
NGC 2859	MJ	2005 Nov 9	1.6	3000	80	no
NGC 2859	MN	2006 May 25	2.5	1800	170	no
NGC 2880	MJ	2009 Nov 16	3.4	2200	142	no
NGC 2880	MN	2009 Dec 18	2.2	2400	52	no
NGC 2964	MJ	2010 Feb 18	1.9	2400	96	yes
NGC 2964	MN	2010 Mar 21	2.2	2400	7	yes
NGC 3031	MJ[b]	2007 Feb 22	2.2	2700	137	yes
NGC 3031	MN[a]	2005 Dec 28	3.1	1800	67	no
NGC 3166	MJ	2008 Feb 6	2.0	2454	85	yes
NGC 3166	MN	2008 Dec 25	2.4	2400	175	no
NGC 3245	MJ	2008 Feb 6	1.7	2700	174	yes
NGC 3245	MN	2008 Dec 25	2.5	2400	84	no
NGC 3351	MJ[b]	2008 Feb 9	1.5	2550	165	yes
NGC 3351	MN	2008 Dec 27	5.0	2400	75	yes
NGC 3368	MJ[b]	2007 Feb 26	3.1	2420	153	yes
NGC 3368	MN[a]	2008 Dec 9	2.6	2400	87	yes
NGC 3384	MJ	2009 Dec 13	1.7	2400	53	yes
NGC 3384	MN	2010 Feb 19	1.8	2400	143	yes
NGC 3521	MJ	2007 Apr 18	1.6	2700	161	yes
NGC 3521	MN	2009 Jan 3	2.3	2528	74	yes
NGC 3593	MJ	2010 Feb 17	1.2	2400	84	yes
NGC 3627	MJ[b]	2006 Dec 27	2.3	1800	10	no
NGC 3627	MN	2007 Feb 23	2.2	1800	100	no
NGC 3675	MJ	2008 Mar 5	2.6	2700	178	yes
NGC 3898	MJ	2007 Apr 19	1.6	2700	108	no
NGC 3945	MJ[b]	2009 Dec 17	2.1	2400	154	yes
NGC 3945	MN	2010 Apr 12	1.6	4200	64	yes
NGC 3953	MJ[b]	2008 Feb 6	2.0	2700	32	yes
NGC 3992	MJ[b]	2008 Dec 28	2.7	2700	66	yes
NGC 4030	MJ	2005 Apr 5	2.3	1800	27	no
NGC 4203	MJ	2007 Apr 12	1.3	2520	7	yes
NGC 4260	MJ	2008 Dec 29	2.7	2700	62	no
NGC 4274	MJ	2007 Apr 19	1.7	2623	99	yes
NGC 4314	MJ	2007 Feb 20	2.3	2700	127	no
NGC 4371	MJ[b]	2006 Dec 27	2.4	1800	85	no
NGC 4371	MN	2006 Jun 19	1.8	1800	175	no
NGC 4379	MJ	2007 Feb 21	2.7	1800	97	yes
NGC 4394	MJ	2007 May 11	1.5	2556	123	yes
NGC 4448	MJ[b]	2007 Apr 16	2.3	2700	85	yes
NGC 4501	MJ	2010 Apr 6	2.0	3340	140	yes
NGC 4501	MN	2010 Apr 8	2.1	2505	50	yes
NGC 4536	MJ	2010 Apr 8	3.6	2385	120	yes
NGC 4536	MN	2010 Apr 10	2.1	2500	30	yes
NGC 4569	MJ	2007 Jun 15	2.1	2700	14	yes
NGC 4569	MN	2010 Apr 12	... [c]	2880	115	yes
NGC 4698	MJ	2008 Dec 28	2.4	2700	166	no
NGC 4736	MJ	2009 Dec 12	1.9	2400	105	yes
NGC 4736	MN[a]	2008 Apr 1	2.2	2700	30	yes
NGC 4772	MJ[b]	2008 Dec 29	2.5	2700	145	no
NGC 4826	MJ[b]	2008 Jan 9	2.0	2187	96	yes
NGC 4826	MN[a]	2009 Jun 25	1.5	2122	25	yes
NGC 5055	MJ	2008 Mar 5	4.0	2700	103	yes
NGC 5055	MN	2009 Jun 26	2.2	2400	13	yes
NGC 5248	MJ[b]	2007 Apr 18	1.6	2700	109	yes
NGC 5566	MJ	2005 Jul 7	2.5	1800	30	no

Table 2
(Continued)

Galaxy	Axis	Date	Seeing (″)	Exp. Time (s)	Angle (°)	Sky
(1)	(2)	(3)	(4)	(5)	(6)	(7)
NGC 5566	MN	2006 May 24	2.0	1750	120	no
NGC 7177	MJ[b]	2007 Aug 11	2.3	2700	60	yes
NGC 7177	MN[a]	2009 Nov 12	1.9	2600	173	yes
NGC 7217	MJ	2007 Aug 12	1.7	2700	81	yes
NGC 7217	MN[a]	2008 Dec 29	1.4	2400	178	no
NGC 7331	MJ	2007 Aug 11	1.7	2700	171	yes
NGC 7743	MJ[b]	2008 Dec 28	2.3	2400	100	no
NGC 7743	MN[a]	2009 Oct 17	2.3	2400	167	no

Notes. (1) Galaxy name. (2) MJ = major axis, MN = minor axis. (3) Date of observation. (4) Seeing FWHM. (5) Total exposure time. (6) Slit position angle east of north. (7) Dedicated sky frame was taken.
[a] MN axis P.A. not orthogonal to MJ axis P.A.
[b] The position angle differs by more than 10° from the Hyperleda published value.
[c] No seeing information available.

Table 3
Observed Kinematic Templates

Identifier (1)	Type (2)	[Fe/H] (3)	Date of Obs. (4)
HR 2600	K2III	−0.35	2005 Mar 4
HR 3369	G9III	0.17	2005 Feb 4
HR 3418	K2III	0.09	2005 Mar 4
HR 3427	K0III	0.16	2005 Mar 4
HR 3428	K0III	0.24	2005 Mar 4
HR 3905	K2IIIb	0.46	2005 Feb 4
HR 6018	K0III-IV	0.01	2005 Feb 4
HR 6159	K7III	−0.13	2005 Feb 4
HR 6770	G8III	−0.05	2005 Mar 4
HR 6817	K1III	−0.06	2005 Feb 4
HR 7576	K3III	0.42	2005 Mar 4

Notes. (1) Identifier. (2) Stellar classification (From Worthey et al. 1994). (3) Metallicity (From Worthey et al. 1994). (4) Date of observation.

4. DATA REDUCTION

We reduce the long-slit spectra following standard procedures of bias subtraction, cosmic ray rejection, and flat fielding under MIDAS described in Mehlert et al. (2000) with additional steps needed to correct for spectral alignment and anamorphism. We correct a two degree tilt between the spectra and the CCD rows by appropriate subpixel shifting of the CCD columns. Two bad columns at positions corresponding to $\lambda = 4850$ Å are corrected through interpolation. We perform the wavelength calibration on neon and cadmium arc frames with typically 10 lines. Where the line signal is low we bin over a few rows along the spatial direction but never over more than five pixels corresponding to 1.2″. After the original line identification we first fit a fourth-order polynomial to the line positions along the spatial direction in order to remove noise-induced row to row jitter, and then fit a third-order polynomial along the spectral direction. The remaining rms scatter in line position is below one pixel. We then rebin the spectra in log-wavelength and correct for anamorphic distortion. The distortion of LRS is measured using stars that are trailed along the slit in order to generate several spectra or *traces* along the whole length of the slit. We centroid the traces by calculating the first moment of the photon count in a 10 pixel wide window around the trace. We first fit a third-order polynomial to describe the trace position as a function of wavelength and then a further third-order polynomial to the trace positions in each column to model the distortion. We find a distortion of up to 10 pixels in the corners of the CCD with respect to the center of the detector (see also Figure 2 in Saglia et al. 2010). We correct for the distortion by means of subpixel shifting. Counts of individual pixels are distributed into pixels of the target frame according the their overlapping surface area. We measure the distortion on several stellar spectra taken in a similar manner on different nights. We find that the residual distortion at the edges of the chip—after correcting one stellar spectra with the distortion information of a different night—is never larger than 1.5″. This is below the typical FWHM of the point-spread function (PSF) of our observations and, more importantly, well below the typical spatial bin sizes that we use at the ends of the slit. To correct for flexure of the instrument during the night we measure the wavelength position of the 5577 Å skyline at the slit ends and correct the wavelength calibration to zeroth order by adding a constant offset. The median absolute offset of all observations is 17 km s^{-1}. Where dedicated sky spectra are available, we collapse them along the spatial direction in order to obtain a single maximum S/N sky spectrum. This spectrum is then scaled according to the exposure time of the object and subtracted from the full frame. In cases where no sky frame is available, the sky signal is determined from the slit ends. One advantage of long-slit spectroscopy is that often the slit ends do contain sufficient nonobject contaminated sky. However, the differential slit illumination is subject to change with time because the HET prime focus assembly moves across the telescope pupil during the duration of an observation. We test the effect of this differential illumination on 44 blank sky spectra obtained over the course of this survey. We use the slit ends to determine the sky signal in the same way as we do for the galaxy spectra. We then determine the differences between those and the sky signal that we measure from the slit center. We find that the residuals amount to no more than 5% of the sky signal in all cases. We then derive kinematics using 5% higher and 5% lower sky values. The resulting errors are significantly smaller than the reported error bars in all cases. In the case of the major axis observation of NGC 3368, NGC 4569, and the minor axis observation of NGC 4569, the use of the dedicated sky frame results in an oversubtraction of the sky (i.e., clearly negative residuals) possibly because of stray light or an increased level of sky background at the time the sky frame was taken. In these cases we use the sky from the slit ends instead. In the cases of large galaxies such as NGC 3031, we test for object contamination by using different window sizes at the slit ends for the sky extraction. We find the effect of object contamination to be negligible in all cases. Finally, all frames go through an extensive visual inspection. Artifacts like residuals of cosmic ray removal are corrected though interpolation of the neighboring pixel.

4.1. Derivation of the Kinematics and Template Library

We derive stellar kinematics using the Fourier Correlation Quotient (FCQ) method of Bender (1990) and Bender et al. (1994). The log-wavelength calibrated and sky-subtracted spectra are spatially binned to reach S/N values of at least 30 pixel^{-1}. An eighth-order polynomial is then fitted to the continuum and the first and last three channels in Fourier space are filtered out

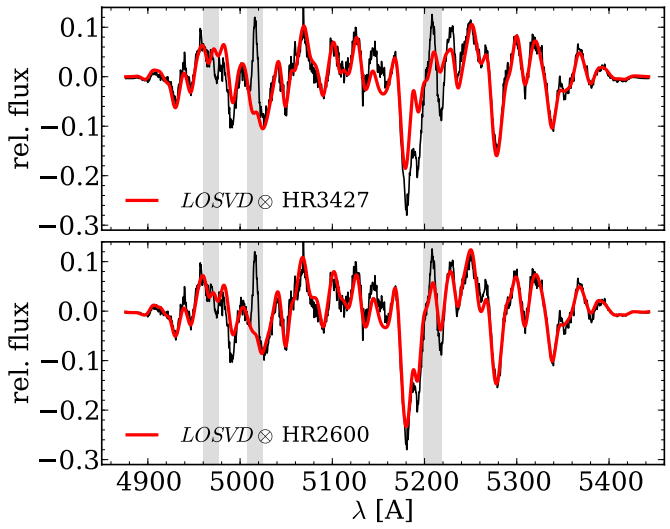

Figure 2. Continuum-removed spectrum in the central radial bin of NGC 2841 (black) and the broadened template spectrum (red). Gray bars mark the positions of the [O III] and [N I] emission lines. Upper panel: choosing the G8III, [Fe/H] = 0.16 star HR3427 results in a notable mismatch around the Mg triplet region. Best-fit parameters are $\sigma = 235.1 \pm 3.0$ km s^{-1}, $h_3 = 0.037 \pm 0.009$, $h_4 = 0.041 \pm 0.009$, rms = 0.034). Lower panel: using HR2600 (K2III, [Fe/H] = −0.35) results in a much better match with $\sigma = 241.2 \pm 3.2$ km s^{-1}, $h_3 = 0.022 \pm 0.009$, $h_4 = 0.048 \pm 0.009$, rms = 0.024. While FCQ finds values for the LOSVD moments that fully agree within the errors, the residual spectrum will look very different for those two cases and render the detection of weak emission lines impossible in the case of HR3427.

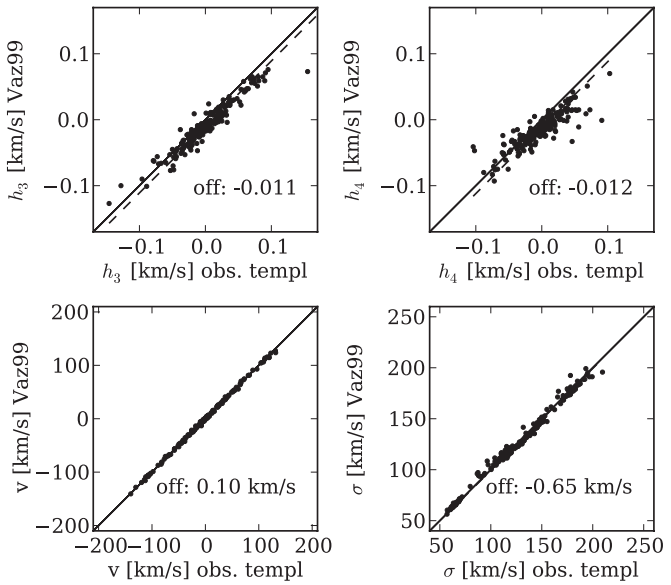

Figure 3. Moments of the LOSVD that we obtain from the kinematic extraction using the Vazdekis SSP library vs. the values that we obtain for the observed templates. The solid lines correspond to a one-to-one correlation; the dashed lines are actual fits to the data. In the case of v and σ the fitted line is covered by the one-to-one line and not visible. Note: we only compare galaxies with no obvious sign of emission.

to remove low and high frequency variations in the continuum level.

FCQ measures the full line-of-sight velocity distribution (LOSVD). By means of deconvolving the autocorrelation function, the FCQ method is more robust against template mismatches than other Fourier- or pixel-space-based methods. Nevertheless, nebular emission lines can significantly affect the derived higher moments of the LOSVDs and therefore need to be taken into account for the derivation of the kinematics. This introduces the necessity of a very accurate model spectrum because otherwise residual mismatches between the observed galaxy spectrum and the broadened model spectrum will mimic emission signatures which are then incorrectly removed. We therefore form a pool of template spectra by combining actual observed stellar spectra (see Table 3) with synthetic simple stellar population (SSP) templates from Vazdekis (1999). Those include varying metallicities and ages. We use a subsample of the published spectra with a Salpeter initial mass function (Salpeter 1955), and all combinations of ages of 1, 2, 5, 10, and 17.78 Gyr and metallicities of [Fe/H] = −1.68, −1.28, −0.68, −0.38, +0.00, +0.20. The published spectral energy distributions have a nominal resolution of 1.8 Å (FWHM) which corresponds to $\sigma^* = 45$ km s^{-1} and therefore slightly lower than the spectral resolution of $\sigma_{\rm inst} = 39.3$ km s^{-1}.

We run FCQ with the collection of all velocity templates. Then we choose the single best-fitting template based on the minimum rms between the broadened template and the galaxy spectrum

$$\mathrm{rms} = \int_{\lambda_1}^{\lambda_2} (G(\lambda) - B(\lambda) \otimes S_i(\lambda))^2 \, d\lambda, \qquad (1)$$

where $\lambda_1 = 4817$ Å to $\lambda_2 = 5443$ Å is the fitted wavelength range, $G(x)$ is the galaxy spectrum, $S_i(x)$ is the ith template spectrum, and $B(x)$ is the broadening function derived from FCQ. Note that this is different from other algorithms such as the Maximum Penalized Likelihood (MPL) technique of Gebhardt et al. (2000) or the Penalized Pixel-Fitting method (pPXF) of Cappellari & Emsellem (2004)) which fit a linear combination of their templates. FCQ subsequently fits Gaussians with Hermite expansions (h_3 and h_4 moments; Gerhard 1993; van der Marel & Franx 1993) to the derived LOSVDs. In Figure 2 we show examples of fits with two different broadened templates. While FCQ indeed finds very similar values for the moments of the LOSVD, the quality of the template match differs significantly in the two cases.

In Figure 3, we compare the impact of the usage of either just our observed templates or just the SSP library. We compare only a subset of galaxies (NGC 2775, NGC 2880, NGC 3675, NGC 4030, NGC 4371 NGC 4379, and NGC 7457) for which we detect no significant emission in order to ensure that the derived moments are not affected by emission. The biases that we introduce by adding the SSP templates to our library are generally small ($\Delta\sigma = -0.65$ km s^{-1}, $\Delta h_3 = -0.011$, $\Delta h_4 = -0.012$) and much smaller than our median errors on the respective moments.

As our spectra often reach into the disk regions we deal with relatively low velocity dispersions. In a few cases the derived dispersions are of the order of the instrumental resolution. The matter gets complicated by the fact that the disk regions are also the regions of lowest surface brightness and therefore the regions with poorest S/N. It is important to understand how reliable the derived moments are under these circumstances.

A caveat of the deconvolution in Fourier space is the amplification of high frequency noise. Fourier-based algorithms therefore filter the signal before the actual deconvolution step. FCQ uses the optimal Wiener filter (Brault & White 1971; Simkin 1974). The basic idea is to decompose the Fourier transform of the input data into a Gaussian contribution—the data part—and an exponential function—the noise part. The *optimal* Wiener

Table 4
Parameters for the Linear Bias Corrections in Velocity Dispersion

Parameter	S/N per pixel			
	22.5	40.0	37.5	75.0
a_σ	1.06	1.06	1.06	1.07
b_σ	−11.04	−10.89	−10.80	−10.70

filter then weighs the various signal channels according to their relative contribution to the data part of the input signal (for details see Bender 1990). While a purely Gaussian LOSVD ought to be well modeled by a Gaussian in Fourier space, the Gauss–Hermite moments cause higher frequency shoulders that are easily *swallowed* by the noise. Adjusting the filter width may recover characteristics of the LOSVD (Bender et al. 1994) at the cost of increased statistical uncertainty.

Here we choose not to broaden the Wiener filter as this yields better stability against statistical deviations, but this causes biases, especially at low velocity dispersions. To correct for these biases we carry out extensive Monte Carlo simulations on a regular parameter grid of velocity dispersion, h_3, h_4, S/N, and template. We generate artificially broadened spectra at each grid point with 30 different noise realizations according to the input S/N. We find that the necessary corrections to σ, h_3, and h_4 are well behaved and linear functions between input and retrieved values and independent of the input template if the velocity dispersion is larger than 75 km s^{-1}, the S/N is larger than 30 pixel^{-1}, and a stellar template is used. The SSP templates cause nonlinear behavior at small velocity dispersions. While we still use the SSP templates to generate broadened model spectra during the emission line fitting, the reported kinematic values are exclusively based on stellar templates, and corrected for biases using

$$\sigma(r) = a_\sigma \cdot \sigma^{\mathrm{FCQ}}(r) + b_\sigma$$
$$h_3(r) = a_{h_3} \cdot {h_3}^{\mathrm{FCQ}}(r) + b_{h_3}$$
$$h_4(r) = a_{h_4} \cdot {h_4}^{\mathrm{FCQ}}(r) + b_{h_4}.$$

Tables 4 and 5 list the corresponding parameters that we obtain from the simulations. For velocity dispersions below 75 km s^{-1} and S/N $<$ 30 pixel^{-1}, we do not report values for h_3 and h_4. Further we report values of v and σ only for S/N $>$ 20.

We estimate statistical errors in the derived moments through Monte Carlo simulations as described in Mehlert et al. (2000). Once the optimum LOSVD is derived by FCQ we generate the synthetic spectra using the fitted v, σ, h_3 and h_4 parameters, and the best-fitting stellar template. In a similar manner as for the bias correction, 100 different realizations of artificial noise are then added to the spectra to reach the same S/N values as in the original spectra. We then use FCQ again to derive the kinematics on those spectra. The reported errors correspond to the statistical 1σ deviations from the mean.

4.2. Emission Line Subtraction and Gas Kinematics

A significant fraction of the objects in our sample show emission in H_β (4861.32 Å), [O III] (4958.83 Å & 5006.77 Å) and [N I] (5197.90 Å & 5200.39 Å). The nitrogen emission line lies on the red flank of the Mg triplet feature—the most important kinematic feature in our spectral range. While typically weak, the nitrogen emission often significantly affects the derivation of h_3 moments. h_3 moments measure the asymmetric deviation from a Gaussian and are expected to behave antisymmetrically

Table 5
Parameters for the Linear Bias Corrections in h_3 and h_4

Parameter	σ	S/N per pixel		
	(km s^{-1})	30.3	37.5	75.0
a_{h_3}	75.0	1.3084	1.2947	1.2734
	100.0	1.1281	1.1142	1.0874
	150.0	1.0182	1.0104	1.0000
	200.0	1.0103	1.0059	0.9988
	250.0	1.0037	1.0008	0.9945
b_{h_3}	75.0	0.0002	0.0001	0.0001
	100.0	0.0003	0.0003	0.0002
	150.0	0.0003	0.0003	0.0003
	200.0	0.0009	0.0008	0.0006
	250.0	0.0010	0.0010	0.0009
a_{h_4}	75.0	1.8521	1.8088	1.7277
	100.0	1.4994	1.4500	1.3555
	150.0	1.0857	1.0655	1.0307
	200.0	1.0407	1.0275	1.0045
	250.0	1.1503	1.1371	1.1089
b_{h_4}	75.0	0.0864	0.0814	0.0738
	100.0	0.0280	0.0240	0.0160
	150.0	0.0165	0.0148	0.0127
	200.0	0.0105	0.0104	0.0104
	250.0	−0.0027	−0.0015	0.0006

with respect to the galaxy center in the case of axisymmetric systems. Deviations from this antisymmetry may hint at contamination by nitrogen emission lines. We therefore decided to remove nebular emission following a procedure similar to the GANDALF routine (Sarzi et al. 2006). We perform a first fit to the galaxy spectrum over a larger spectral range reaching from 4820 Å to 5440 Å using the FCQ algorithm. We then subtract the best-fitting broadened stellar spectrum from the galaxy spectrum and fit Gaussian functions—using a standard least squares algorithm—to the residual emission. The algorithm first searches for emission in a 500 km s^{-1} window around the brighter oxygen line at 5007 Å (the oxygen doublet is well resolved at our instrumental resolution) redshifted to the systemic velocity. It fits for the three parameters of amplitude, central velocity, and the velocity dispersion. It then goes on to the other and generally weaker emission lines and performs a fit to their amplitude while assuming the same central velocity and velocity dispersion as the oxygen line. In principle the ratio of the two oxygen emission lines is given by atomic physics and is a constant of value 0.33. Rather than fixing these values during the fit we also fit the lower amplitude line as this provided another handle on the reliability of our method. We then subtract the best-fitting emission lines from the original galaxy spectrum and repeat the FCQ multiple-template fit. The best-fitting broadened template is again subtracted from the input spectrum and the gas emission fit is repeated on the improved difference spectrum. An example for a spectrum that shows signs of nebular emission is shown in the upper panel of Figure 4. We plot the residuals between the recorded spectrum and the broadened model spectrum after the removal of the emission in the lower panel. This iterative approach was found to converge very quickly. A fourth FCQ fit typically yields no further significant change in the derived kinematics. Our reported stellar kinematics went through three subsequent iterations of template fitting with two interleaved gas emission removal steps. The gas removal routine gives access to the study of line ratios (Sarzi et al. 2006) and is also a

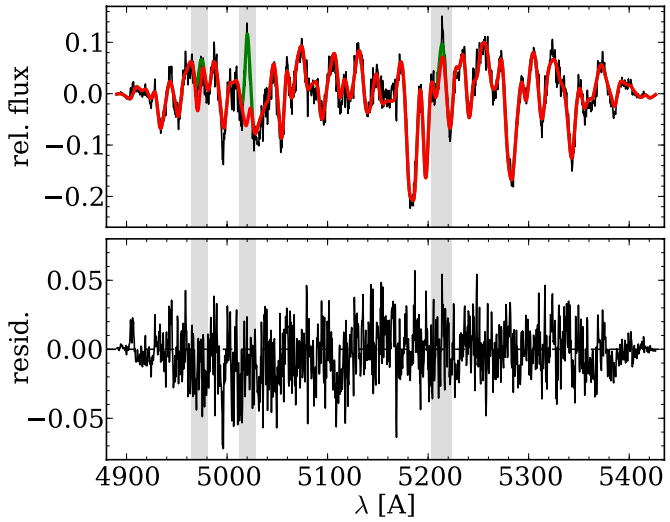

Figure 4. Example of the nebular emission line subtraction. Here the gas emission was removed from one of the central spectra of NGC 3368. Upper panel: after subtraction of the best-fitting broadened stellar template (red) the algorithm finds a significant emission signal in the [O III] lines and the nitrogen doublet (green). The vertical bars mark the search range for emission. Lower panel: residuals between observed and model spectrum after removal of the emission.

necessary step before the calculation of absorption line indices and subsequent stellar population analysis, both of which will be the subject of a forthcoming publication.

4.3. Identification of Pseudobulges

If no classification is already available from Fisher & Drory (2008, 2010), we follow the same procedure for the identification of pseudobulges. We define a bulge photometrically as the excess light over the inward extrapolation of the outer disk exponential luminosity profile. The bulge-to-disk decompositions that we adopt in Section 4.4 allow us to determine the bulge region of an object. Here, we classify bulges using close to *V*-band *Hubble Space Telescope* (*HST*) images (F547M, F555W, and F606W). While these bands are subject to dust obscuration they are also sensitive to an enhancement in star formation rate, a feature commonly observed in pseudobulges (Fisher 2006). We visually inspect the *HST* images to see whether the bulge regions contain disk-like structures such as nuclear spirals, nuclear bars, and/or nuclear rings. If such structures are present we call the photometric bulge a pseudobulge. If there is no structure (the bulge resembles an elliptical galaxy with a smooth light distribution), we call this bulge a classical bulge.

Weak central dust spirals that also occur frequently in elliptical galaxies (e.g., Storchi-Bergmann et al. 2007)—often distinguishable from the outer disk because they are inclined differently—are no reason for us to call a bulge a pseudobulge. NGC 2841 poses an example for this situation. A dust spiral can easily be identified in *HST* F438W, but it is misaligned with the outer disk also seen only in the vicinity of the nucleus.

Yet, a few objects remain for which we do not feel confident assigning a classification based on their *HST* morphology: NGC 2460, NGC 3953, NGC 4826, and NGC 7217. We treat them as unclassified throughout this work. As mentioned in Section 2, we also do not classify the bulges of the galaxies NGC 3593 and NGC 7331 due to their high inclination. In Appendix B we give a detailed explanation for the bulge classification for each individual object.

4.4. Photometry

We use the results from decompositions of surface brightness profiles to investigate possible correlations between photometric parameters and kinematic structure. Also the bulge-disk decompositions serve to identify the actual bulge region of a particular galaxy.

We derive surface photometry following the prescriptions in Fisher & Drory (2008, 2010). For each galaxy, we combine multiple data sources mostly in the infrared (but sometimes in optical bands) to obtain a final one-dimensional composite surface brightness profile. The different data have been calibrated against the *H*-band using Two Micron All Sky Survey (2MASS) magnitudes. High-resolution *HST* imaging is used in the galaxy center, while wide-field images sample the outer disk. The resulting composite profile of each galaxy is used to derive the bulge-to-disk photometric decomposition. Our method is well tested and has been used in several publications (Fisher & Drory 2008, 2010; Kormendy et al. 2009). Our principal source of data is 2MASS *H*-band maps (Skrutskie et al. 2006). When available we use data from the 2MASS Large Galaxy Atlas (Jarrett et al. 2003). We prefer the *H* band over K_s because the 2MASS *H*-band data are more sensitive than the 2MASS K_s data. For all galaxies we use the NASA/IPAC Extragalactic Database to search for ancillary ground-based *H*-band data. We also include *Spitzer* 3.6 μm data. Finally, when available, we also include high-resolution F160W images from *HST*/NICMOS. In a few cases, where galaxies were lacking archival NICMOS data, we use *I*- or *R*-band data instead. The high-resolution data can be crucial to accurately constraining the bulge-disk decomposition. Fisher & Drory (2010) investigated the uncertainty introduced from mixing filters in this way. It is typically smaller than 0.1 mag, and therefore small compared to the uncertainty in the fit. Also, Fisher & Drory (2008) derived very similar Sérsic indices with *V*-band data as with *H*-band profiles.

We fit ellipses to all images. Isophotal fitting is carried out using the code of Bender & Moellenhoff (1987). See Fisher & Drory (2008) for a brief summary of the procedure. The code returns a two-dimensional surface brightness profile (including major & minor axis size, position angle, and mean surface brightness for each ellipse center). We then combine all profiles into a composite surface brightness profile. The power of this method is two-fold. First, a combination of surface brightness profiles allows us to robustly identify systematic errors from PSFs and sky subtraction. Second, the resulting composite profile has an extremely high dynamic range in radius, which is necessary to accurately constrain the bulge-disk decomposition (see discussion in the Appendix of Fisher & Drory 2008 and also Kormendy et al. 2009). The zero points of our profiles are matched against the 2MASS data.

We determine bulge and disk parameters by fitting each surface brightness profile with a one-dimensional Sérsic function plus an exponential outer disk,

$$I(r) = I_0 \exp\left[-(r/r_0)^{1/n}\right] + I_d \exp\left[-(r/h)\right], \qquad (2)$$

where r represents the distance along the major axis, I_0 and r_0 are the central surface brightness and scale length of the bulge, I_d and h represent the central surface brightness and scale length of the outer disk, and n represents the bulge Sérsic index (Sérsic 1968). The half-light radius, r_e, of the bulge is obtained by converting r_0,

$$r_e = (b_n)^n r_0, \qquad (3)$$

Table 6
Data Sources

No.	Instrument	Filter	Scale (arcsec pixel^{-1})	Field of View (arcsec)	Reference
1	*HST* NICMOS 1	F160W	0.043	11 × 11	MAST archive[a]
2	*HST* NICMOS 2	F160W	0.075	19.2 × 19.2	MAST archive[a]
3	*HST* NICMOS 3	F160W	0.20	51.2 × 51.2	MAST archive[a]
4	2MASS	*H*	1.0	512 × 1024	IPAC archive
5	2MASS	*H*	1.0	variable size, mosaic	Jarrett et al. (2003)
6	*Spitzer* IRAC	3.6 μm	0.60	variable size, scan	IPAC archive[b]
7	*Spitzer* IRAC (SINGS)	3.6 μm	0.75	variable size, scan	SINGS[c]
8	*HST* ACS/WFC	F814W	0.049	202 × 202	MAST archive[a]
9	*HST* WFPC2	F547M	0.10	80 × 80	MAST archive[a]
10	*HST* WFPC2	F814W	0.10	80 × 80	MAST archive[a]
11	Perkins 1.8 m OSIRIS	*H*	1.5	412 × 412	Eskridge et al. (2002)
12	Lick 3 m pNIC	*K*	0.24	15.4 × 15.4	Rauscher (1995)
13	CTIO 1.5 m OSIRIS	*H*	1.1	312 × 312	Eskridge et al. (2002)
14	William Herschel Telescope INGRID	*K*	0.24	252 × 252	Knapen et al. (2003)
15	Calar Alto Observatory 2.2 m MAGIC NICMOS 3	*K*	0.66	172 × 172	Möllenhoff & Heidt (2001)
16	Mauna Kea 0.61 m NICMOS 256	*K*	2.1	644 × 568	Tully et al. (1996)
17	UKIRT 3.8 m IRCAM II	*H*	1.7	198 × 72	de Jong & van der Kruit (1994)

Notes.
[a] http://archive.stsci.edu/
[b] http://irsa.ipac.caltech.edu/
[c] http://data.spitzer.caltech.edu/popular/sings/

where the value of b_n is a proportionality constant defined such that $\Gamma(2n) = 2\gamma(2n, b_n)$ (Ciotti 1991). Γ and γ are the complete and incomplete gamma functions, respectively. We use the approximation $b_n \approx 2.17n - 0.355$ (Caon et al. 1993). We restrict our range in possible Sérsic indices to $n > 0.33$ to ensure that the approximation is accurate. Bulge and disk magnitudes are adjusted to account for the shape of the bulge using the ellipticity profile from the isophote fitting.

Intermediate-type galaxies are known to contain many components that are not well described by the decomposition into a Sérsic bulge and exponential disk (e.g., bars, rings, nuclear star clusters). Similar to the outer disk, in the bulge we exclude significant non-Sérsic components such as nuclear bars and nuclear rings. The inclusion of these features can have unpredictable effects on the Sérsic index, depending on the relative size of the feature, and what type it is. The appendix of Fisher & Drory (2008) discusses how masking data in the bulge will affect the decomposition. Essentially, this has the effect of decreasing the robustness of the fit, which will be reflected in the error bars. The parameters from the decompositions are presented in Table 7, and the image data sources are described in Table 6.

The surface brightness profile of NGC 5566 does not follow a typical bulge/disk profile. We publish the obtained kinematics here but exclude this object from all further analysis.

4.5. Bulge Radius

Here we are particularly interested in the kinematic properties of the bulge regions of our observed galaxies. Of course the derived LOSVDs will always be the light-weighted average of all components (bulge, disk, bar) along a particular line of sight through the galaxy, but the photometric bulge-to-disk decompositions allow us to determine within which radius the bulge should dominate. We define the *bulge radius* r_b along the major axis as the radius where the light contribution of the photometric bulge component exceeds the light contribution of the disk component by 25%:

$$I_0^{\rm bulge} \exp\left(-\left(\frac{r_b}{r_0}\right)^{\frac{1}{n}}\right) = 1.25 \cdot I_0^{\rm disk} \exp\left(-\frac{r_b}{h}\right), \quad (4)$$

where $I_0^{\rm bulge}$ is the central surface brightness of the bulge component, $I_0^{\rm disk}$ is the central surface brightness of the disk component, r_0 and h are the scale lengths of the bulge and disk components, and n is the Sérsic index (see previous section for the relation between r_0 and r_e). One might argue that the bulge effective radius r_e is a more natural choice as r_b of course is dependent on the disk parameters, but we find that in a number of galaxies r_e actually lies in a region that is dominated by disk light. The choice of 25% is a compromise between the desire to be reasonably dominated by the bulge component on the one hand and still wanting to maintain a sufficient number of resolution elements within the bulge radius on the other. The values for the bulge radius are listed in Table 9. In Figure 16 we indicate the location of the bulge radius though a dashed vertical line.

5. RESULTS

5.1. Kinematic Profiles and Comparison with Literature

Table 8 gives an example of the format of the measured stellar kinematic moments as a function of the distance from the center of the galaxy. The full listing is available electronically[6]. In Appendix A we plot the kinematic profiles. When available, we also plot data from the literature for comparison. Integral Field Spectroscopic data from SAURON are available for some of the galaxies in our sample. In those cases we create pseudo long-slit data through interpolation of the SAURON v, σ, h_3, and h_4 maps along a slit aperture with a position angle corresponding to our observation. In general the agreement of our data with the published values is acceptable.

[6] http://cds.u-strasbg.fr/

Table 7
Bulge-to-disk Decomposition Parameters[a]

Galaxy	Bulge Morph.	n	μ_e (mag arcsec^{-2})	r_e (arcsec)	$m^{\rm Sérsic}$ (mag)	$\mu_0^{\rm disk}$ (mag arcsec^{-2})	h (arcsec)	$m^{\rm disk}$ (mag)	Data Sources
(1)	(2)	(3)	(4)	(5)	(6)	(7)	(8)	(9)	(10)
NGC 1023	c	2.52 ± 0.81	15.76 ± 1.11	12.35 ± 4.39	7.15 ± 1.11	16.62 ± 0.32	62.20 ± 6.56	5.66 ± 0.35	5,10,15
NGC 2460	p	3.49 ± 0.32	18.02 ± 0.46	12.69 ± 4.40	9.19 ± 0.46	16.40 ± 0.28	11.42 ± 0.98	9.11 ± 0.31	2,4
NGC 2681	p	3.82 ± 0.31	14.58 ± 0.63	3.74 ± 3.00	8.35 ± 0.63	17.32 ± 0.33	23.78 ± 2.76	8.44 ± 0.37	3,4,6
NGC 2775	c	3.23 ± 0.93	17.28 ± 1.02	15.86 ± 5.50	8.00 ± 1.02	17.20 ± 0.61	41.28 ± 7.91	7.12 ± 0.67	4,6,10,11,14,15
NGC 2841	c	3.22 ± 0.58	16.55 ± 0.68	15.46 ± 8.98	7.33 ± 0.68	16.49 ± 0.17	60.51 ± 2.82	5.58 ± 0.18	2,5,7
NGC 2859	c	2.34 ± 0.65	16.23 ± 1.08	8.3(<21.4[b])	8.52 ± 1.08	19.11 ± 0.47	55.17 ± 8.93	8.41 ± 0.52	5,6,8
NGC 2880	c	3.41 ± 0.48	17.49 ± 0.59	11.7(<24.2[b])	8.85 ± 0.59	18.29 ± 0.40	25.47 ± 1.88	9.26 ± 0.41	4,10
NGC 2964	p	1.01 ± 0.34	15.43 ± 0.51	2.04 ± 0.50	11.18 ± 0.51	16.40 ± 0.18	16.07 ± 0.65	8.37 ± 0.19	2,4,6
NGC 3031	c	4.09 ± 0.48	17.14 ± 0.62	70.70 ± 54.91	4.49 ± 0.62	16.59 ± 0.25	132.80 ± 8.05	3.98 ± 0.26	2,5,7
NGC 3166	p	1.24 ± 0.30	14.37 ± 0.39	4.36 ± 1.12	8.37 ± 0.39	15.86 ± 0.44	15.47 ± 2.66	7.92 ± 0.50	5,6,9,11
NGC 3245	c	2.75 ± 0.56	15.16 ± 0.80	4.51 ± 1.70	8.69 ± 0.80	16.44 ± 0.28	21.60 ± 1.49	7.77 ± 0.30	2,4,6
NGC 3351	p	1.38 ± 0.74	15.99 ± 0.60	8.08 ± 3.10	8.59 ± 0.60	17.01 ± 0.44	49.48 ± 5.13	6.54 ± 0.47	2,5,7
NGC 3368	p	2.46 ± 0.77	15.97 ± 0.75	13.08 ± 7.29	7.25 ± 0.75	16.57 ± 1.95	35.26 ± 29.61	6.84 ± 2.31	2,4,7
NGC 3384	p	1.58 ± 0.22	14.39 ± 0.40	5.35 ± 1.16	7.83 ± 0.40	16.96 ± 0.15	44.42 ± 3.13	6.73 ± 0.18	2,5,6
NGC 3521	c	3.66 ± 0.77	15.48 ± 1.50	8.55 ± 6.36	7.48 ± 1.50	15.99 ± 0.31	49.53 ± 3.87	5.52 ± 0.33	2,5,7
NGC 3593	?	1.22 ± 0.21	16.18 ± 0.27	14.55 ± 2.16	7.57 ± 0.27	17.61 ± 0.30	52.52 ± 4.99	7.02 ± 0.33	3,5,6,11
NGC 3627	p	1.50 ± 0.58	14.53 ± 0.59	4.77 ± 1.52	8.24 ± 0.59	16.72 ± 0.15	65.99 ± 0.15	5.63 ± 0.16	3,5,7
NGC 3675	p	1.57 ± 1.12	16.35 ± 1.93	9.0(<23.4[b])	8.66 ± 1.93	16.22 ± 0.31	36.85 ± 3.42	6.40 ± 0.34	2,5,6,11
NGC 3898	c	3.22 ± 0.86	15.93 ± 1.27	7.63 ± 2.88	8.24 ± 1.27	17.25 ± 0.64	29.00 ± 4.56	7.94 ± 0.68	2,5,6
NGC 3945	p	1.79 ± 0.48	16.00 ± 0.76	9.82 ± 3.50	8.05 ± 0.76	19.02 ± 0.44	83.17 ± 26.76	7.43 ± 0.64	5,6,10
NGC 3953	?	2.43 ± 0.68	17.15 ± 0.96	12.74 ± 8.03	8.49 ± 0.96	17.44 ± 0.15	66.14 ± 4.73	6.34 ± 0.19	2,3,5,7
NGC 3992	c	3.18 ± 1.18	17.44 ± 1.44	12.23 ± 3.74	8.73 ± 1.44	17.65 ± 0.50	77.54 ± 19.36	6.20 ± 0.62	5,9,16
NGC 4030	p	1.98 ± 1.30	16.50 ± 1.52	5.18 ± 2.14	9.89 ± 1.52	15.60 ± 0.36	15.82 ± 1.95	7.61 ± 0.41	2,4,6,13
NGC 4203	c	2.45 ± 0.83	15.72 ± 1.51	6.78(<15.9[b])	8.43 ± 1.51	17.28 ± 0.37	30.31 ± 3.53	7.88 ± 0.41	4,6,10
NGC 4260	c	3.68 ± 0.42	19.08 ± 0.48	21.49 ± 11.93	9.08 ± 0.48	17.02 ± 0.19	21.69 ± 1.59	8.34 ± 0.22	2,4,6
NGC 4274	p	1.52 ± 0.24	15.49 ± 0.28	5.92 ± 1.10	8.73 ± 0.28	17.03 ± 0.16	46.53 ± 2.92	6.70 ± 0.19	5,6,8
NGC 4314	p	2.72 ± 0.96	17.12 ± 1.09	10.53 ± 6.96	8.82 ± 1.09	16.70 ± 0.36	35.08 ± 2.65	6.98 ± 0.38	2,4,6,14
NGC 4371	p	2.21 ± 1.00	16.66 ± 1.35	10.97 ± 6.00	8.37 ± 1.35	18.10 ± 0.98	44.59 ± 13.45	7.86 ± 1.07	1,4,6
NGC 4379	c	2.39 ± 0.55	16.72 ± 0.69	6.40 ± 1.97	9.56 ± 0.69	16.91 ± 0.37	13.52 ± 1.48	9.26 ± 0.40	1,4,8
NGC 4394	p	1.58 ± 0.67	16.28 ± 0.87	6.10 ± 1.81	9.43 ± 0.87	18.40 ± 0.25	57.75 ± 6.38	7.60 ± 0.30	4,6,11,12
NGC 4448	p	1.19 ± 0.25	16.43 ± 0.31	6.70 ± 1.01	9.52 ± 0.31	16.85 ± 0.17	28.42 ± 0.97	7.59 ± 0.18	5,6,10,11
NGC 4501	p	1.25 ± 1.06	15.43 ± 1.34	5.31 ± 1.53	8.99 ± 1.34	15.81 ± 0.46	39.26 ± 3.89	5.85 ± 0.49	5,6,12
NGC 4536	p	1.47 ± 0.35	14.77 ± 0.62	3.98 ± 1.18	8.88 ± 0.62	17.18 ± 0.15	32.32 ± 1.82	7.64 ± 0.17	2,5
NGC 4569	p	2.34 ± 0.97	15.13 ± 1.59	4.80 ± 2.33	8.60 ± 1.59	16.84 ± 0.32	61.32 ± 6.42	5.91 ± 0.36	2,3,5,7
NGC 4698	c	2.51 ± 0.53	15.66 ± 0.66	5.11 ± 1.41	8.97 ± 0.66	17.32 ± 0.34	34.93 ± 2.76	7.61 ± 0.36	2,4,6,11
NGC 4736	p	1.23 ± 0.30	13.80 ± 0.41	7.76 ± 1.65	6.56 ± 0.41	14.93 ± 0.35	26.82 ± 3.85	5.80 ± 0.41	3,5,7
NGC 4772	c	3.03 ± 0.88	17.73 ± 1.20	13.49 ± 8.24	8.84 ± 1.20	18.87 ± 0.55	71.96 ± 16.04	7.59 ± 0.64	4,11
NGC 4826	?	3.93 ± 0.88	16.93 ± 1.06	28.93 ± 10.26	6.25 ± 1.06	16.50 ± 0.27	67.95 ± 6.86	5.34 ± 0.31	2,5,7
NGC 5055	p	1.71 ± 1.03	17.35 ± 1.36	27.88 ± 16.08	7.16 ± 1.36	16.57 ± 0.38	68.70 ± 5.53	5.40 ± 0.40	3,5,7
NGC 5248	p	1.29 ± 0.45	16.47 ± 0.67	0.7(<4.9[b])	8.74 ± 0.67	17.43 ± 0.28	43.99 ± 3.72	7.21 ± 0.30	2,5,6
NGC 7177	p	2.03 ± 0.52	16.35 ± 0.59	7.02 ± 3.17	9.08 ± 0.59	16.42 ± 0.31	15.45 ± 0.73	8.49 ± 0.32	2,4,6,17
NGC 7217	?	3.20 ± 1.03	17.04 ± 1.21	13.41 ± 9.35	8.13 ± 1.21	16.50 ± 0.64	28.54 ± 6.60	7.23 ± 0.72	2,4,6,11
NGC 7331	?	2.85 ± 1.02	16.20 ± 1.30	16.63 ± 9.90	6.88 ± 1.30	16.97 ± 0.47	61.61 ± 9.04	6.03 ± 0.52	3,5,7
NGC 7743	p	3.66 ± 0.52	15.15 ± 0.89	2.37 ± 1.04	9.94 ± 0.89	17.14 ± 0.22	22.27 ± 1.96	8.41 ± 0.25	2,4,6

Notes. (1) Galaxy name. (2) Bulge classification: c = classical, p = pseudobulge, ? = not classified. (3) Bulge Sérsic index. (4) Bulge surface brightness at r_e. (5) Bulge effective radius along the major axis. (6) Bulge apparent magnitude. (7) Disk central surface brightness. (8) Disk scale length. (9) Disk apparent magnitude. (10) Image data sources, see Table 6.

[a] These photometric decompositions are based on infrared and optical data, but calibrated against the H band.

[b] The error on the effective radius is comparable to or larger than the value itself. We list the value that is preferred by the fit and the upper limit.

Table 8
Format Example of the Measured Stellar Kinematics

Galaxy	P.A. (deg)	r ($''$)	v (km s^{-1})	σ (km s^{-1})	h_3	h_4
(1)	(2)	(3)	(4)	(5)	(6)	(7)
NGC 1023	87	51.46	186.55 ± 2.71	92.16 ± 2.55	−0.067 ± 0.017	−0.037 ± 0.015

Notes. (1) Identifier. (2) Observed position angle. (3) Distance from the center (positive: east; negative: west). (4) Velocity relative to systemic velocity. (5) Velocity dispersion. (6) Gauss–Hermite h_3 moment. (7) h_4 moment. The full listing is available electronically (http://cds.u-strasbg.fr/).

Table 9
Structural and Kinematic Parameters

Galaxy	$r_{\mu_b=\mu_d}$ (arcsec)	r_b (arcsec)	$\langle\epsilon_b\rangle$	$\langle\epsilon_d\rangle$	$\sigma_{r_e/10}$ (km s^{-1})	γ_{MJ}	δ_{MJ}	γ_{MN}	δ_{MN}	$\frac{\langle v^2\rangle}{\langle\sigma^2\rangle}$
(1)	(2)	(3)	(4)	(5)	(6)	(7)	(8)	(9)	(10)	(11)
NGC 1023	21.3	19.0	0.22	0.55	212.9 ± 5.2	−0.09	1.12	−0.17	1.176	0.165
NGC 2460	8.3	6.6	0.19	0.25	111.4 ± 3.5	−0.01	0.99	0.10	1.026	0.358
NGC 2681	14.6	13.2	0.11	0.20	112.5 ± 1.3	−0.16	1.19	...	...	... [a]
NGC 2775	19.4	16.8	0.10	0.16	173.9 ± 13.7	−0.04	1.02	1.03	1.027	0.133
NGC 2841	17.4	15.2	0.22	0.49	222.2 ± 19.3	−0.11	1.15	−0.09	1.124	0.207
NGC 2859	30.0	27.6	0.16	0.22	176.8 ± 5.4	−0.06	1.11	−2.04	1.379	0.678
NGC 2880	26.7	22.7	0.20	0.35	142.2 ± 5.3	−0.21	1.35	−0.22	1.394	0.496
NGC 2964[b]	3.4	3.1	0.15	0.28	88.4 ± 1.3	...	...	...	...	0.117
NGC 3031	72.0	61.3	0.24	0.43	157.5 ± 13.6	−0.06	1.03	−0.03	1.006	0.400
NGC 3166	9.9	9.1	0.39	0.25	151.4 ± 6.1	0.00	1.04	0.05	0.981	1.365
NGC 3245	9.5	8.5	0.20	0.44	225.2 ± 8.3	−0.21	1.27	−0.22	1.184	0.300
NGC 3351	14.2	12.9	0.16	0.24	90.0 ± 4.2	0.05	1.01	−0.05	1.015	0.778
NGC 3368	23.3	20.4	0.17	0.34	122.5 ± 6.6	−0.01	0.99	0.03	0.883	0.574
NGC 3384	15.5	14.4	0.20	0.34	150.3 ± 2.4	−0.09	1.10	−0.13	1.150	0.521
NGC 3521	12.2	10.8	0.35	0.45	129.5 ± 2.9	−0.01	0.99	−0.14	1.098	0.905
NGC 3593	32.1	29.5	0.49	0.62	62.3 ± 3.1	0.20	0.70	...	...	0.065
NGC 3627	11.7	10.9	0.27	0.51	116.1 ± 3.9	−0.05	1.03	0.01	1.003	0.267
NGC 3675	9.8	8.5	0.29	0.49	114.7 ± 5.3	−0.03	1.03	...	...	0.363
NGC 3898	17.7	15.7	0.25	0.41	219.0 ± 8.3	−0.14	1.21	...	...	0.295
NGC 3945	33.3	31.0	0.19	0.17	183.1 ± 5.4	−0.03	1.12	−0.11	1.088	1.062
NGC 3953	16.6	14.6	0.26	0.48	110.6 ± 3.1	0.02	0.95	...	...	0.178
NGC 3992	14.9	13.2	0.22	0.49	144.2 ± 9.5	0.07	0.97	...	...	0.406
NGC 4030[b]	3.6	3.0	0.11	0.19	102.9 ± 4.5	...	...	...	...	0.213
NGC 4203	16.4	14.7	0.11	0.11	170.1 ± 3.6	−0.18	1.31	...	...	0.249
NGC 4260	9.0	7.3	0.21	0.53	143.8 ± 14.3	0.03	0.98	...	...	0.131
NGC 4274	12.3	11.3	0.40	0.34	106.9 ± 5.3	0.08	0.90	...	...	0.842
NGC 4314	10.0	8.6	0.12	0.45	123.3 ± 5.1	−0.01	1.00	...	...	0.825
NGC 4371	25.5	22.9	0.29	0.33	125.8 ± 5.0	−0.12	1.20	0.00	0.983	0.426
NGC 4379	10.0	8.6	0.11	0.20	121.0 ± 4.6	−0.20	1.16	...	...	0.183
NGC 4394	15.2	14.1	0.12	0.37	80.0 ± 3.1	−0.01	0.91	...	...	1.451
NGC 4448	9.6	8.5	0.26	0.43	98.5 ± 3.7	−0.03	1.03	...	...	0.446
NGC 4501	7.0	6.2	0.19	0.45	144.2 ± 4.9	0.00	1.01	0.07	0.937	0.390
NGC 4536	10.9	10.1	0.39	0.47	98.1 ± 3.3	−0.06	1.01	0.10	0.942	0.724
NGC 4569	10.6	9.6	0.32	0.57	114.4 ± 0.9	−0.05	1.04	...	...	0.525
NGC 4698	11.9	10.7	0.20	0.27	139.3 ± 10.4	−0.05	1.03	...	...	0.008
NGC 4736	15.6	14.2	0.11	0.17	107.0 ± 2.3	−0.09	1.15	−0.17	1.199	1.330
NGC 4772	26.3	23.5	0.06	0.42	144.5 ± 8.1	−0.12	1.22	...	...	0.060
NGC 4826	29.5	25.4	0.23	0.42	95.7 ± 6.4	0.01	1.00	−0.04	1.080	0.375
NGC 5055	22.0	18.3	0.26	0.39	106.1 ± 8.6	−0.03	1.04	−0.02	1.031	0.471
NGC 5248	17.0	15.4	0.23	0.37	78.4 ± 2.5	...	...	...	...	0.620
NGC 5566[c]	...	...	...	...	148.9 ± 2.2[d]	...	...	...	...	...
NGC 7177	10.0	8.6	0.17	0.32	115.3 ± 4.8	−0.03	1.02	...	...	0.508
NGC 7217	13.2	11.2	0.05	0.10	141.1 ± 12.7	0.00	1.02	−0.08	1.100	0.168
NGC 7331	29.4	26.0	0.39	0.59	123.6 ± 13.0	−0.11	1.23	...	...	1.520
NGC 7743	6.2	5.6	0.11	0.31	84.6 ± 2.4	−0.01	1.02	...	...	0.069

Notes. Structural and kinematic parameters for the galaxies in our sample. (1) Target name. (2) Radius of equal bulge and disk surface brightness. (3) Adopted bulge radius for this study. (4) Mean apparent bulge ellipticity. (5) Mean apparent disk ellipticity. (6) Central velocity dispersion averaged within one-tenth of the bulge effective radius. (7) Slope of major axis velocity dispersion profile. (8) Major axis ratio of the averaged velocity dispersion within the annulus $r < r_b/3$ to averaged dispersion within $r_b/3 < r < r_b$. (9) Slope of minor axis velocity dispersion profile. (10) Minor axis ratio of velocity dispersion. (11) $\langle v^2\rangle/\langle\sigma^2\rangle$ (Binney 2005) for the inclination corrected velocity.

[a] The low inclination of this galaxy prevents us from deriving an inclination corrected velocity and hence $\langle v^2\rangle/\langle\sigma^2\rangle$.

[b] The bulge is not sufficiently resolved to calculate the slopes of the velocity dispersion.

[c] Surface brightness does follow a typical bulge/disk profile. We do not decompose the profile and only present the kinematics data here.

[d] No decomposition; this is the innermost value.

In a few cases, such as NGC 4203, a difference between the previously published data and ours are explained by the difference in the observed position angle.

Bertola et al. (1995) find somewhat larger velocity dispersions for NGC 4379 than we do. Formally their instrumental dispersion should allow us to resolve the 80 km s^{-1}–118 km s^{-1} that we find for the dispersion in the bulge.

Dumas et al. (2007) find larger velocity dispersions in the cases of NGC 3351 and NGC 5248 than we do. The dispersion of those objects is probably too low to be resolved by their instrumental dispersion of ≈110. km s^{-1}.

Vega Beltrán et al. (2001) find systematically lower velocity dispersions for NGC 2841 than we do. However, we also plot data from Héraudeau & Simien (1998) which are in excellent agreement with ours.

The SAURON data for NGC 4698 (Falcón-Barroso et al. 2006) suggest a somewhat larger velocity dispersion over our whole observed range than we find. They also find negative h_3 moments on the east side. The dispersion of this galaxy ($\approx$140 km s^{-1}) should be well resolved by SAURON and as such the difference remains somewhat mysterious but small.

5.2. Signatures of Bars in Velocity Profiles

In our sample, 29 out of 45 of the galaxies are classified as barred or as hosting an oval. Bars and ovals will affect the observed kinematics and their presence should be reflected in the moments of the observed LOSVD. Bureau & Athanassoula (2005) use N-body simulations to derive diagnostics for the presence of bars in edge-on disks. They find that double hump rotation curves, plateaus and shoulders in velocity dispersion, and correlation of h_3 moments with velocity in contrast to the usually seen anti-correlation are indicators for the presence of a bar. The double hump describes a rotation curve that first rises quickly with radius, reaches a local maximum, then drops slightly and starts rising again toward larger radii. We do see similar features in a number of our galaxies even though they are not observed edge-on (e.g., see the rotation curves for NGC 2841, NGC 3351, and NGC 3384 in Figure 16). The signature is not always strong enough to form an actual local minimum after the fast inner rise. Instead, in some cases we observe shelves: the rise in velocity stagnates for a certain radial range but becomes larger again before finally flattening out (e.g., NGC 1023 and NGC 3627 in Figure 16).

Out of 29 barred galaxies (including 6 ovals), 20 do show such features. However, our data do not extend very far into the disk region in many of the objects in our sample; also visibility may be inhibited by the coarse spatial binning of some of our spectra. Further, this diagnostic tool was developed for edge-on systems, so it is likely that we miss bar signatures in the velocity profiles. However, 9 of the 16 nonbarred galaxies show either shelves or double humps which may be an indication that those systems actually do host a bar that is not readily seen photometrically.

5.3. Central Velocity Dispersions

We calculate the central velocity dispersion of the galaxies in our sample by averaging the major axis dispersion within a tenth of the effective bulge radius r_e that we obtain from the photometric decomposition. The values for the central dispersions are given in Table 9. The quoted errors correspond to the formal errors of the derived mean within $r_e/10$.

In Figure 5 we show corresponding histograms of the central dispersions. In the left panel we discriminate bulge types based on their morphology, in the right panel we discriminate by Sérsic index. There is significant overlap between the distributions of velocity dispersions for the classical and pseudobulges. Nonetheless, it is clear that, in our sample, pseudobulges have, on average, lower velocity dispersions. We find in our sample that classical bulges become exceedingly rare below central velocity dispersions of 100 km s^{-1}. However, we caution that our sample is not volume-limited.

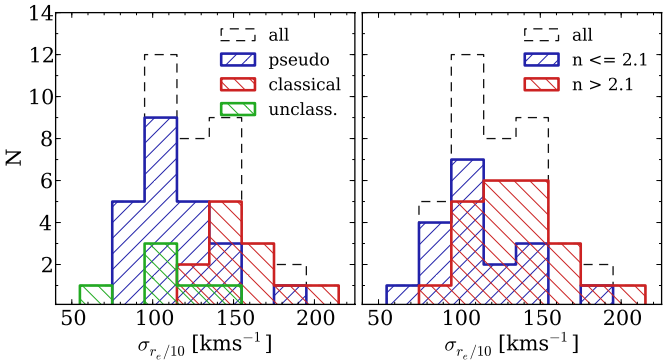

Figure 5. Histograms of the central velocity dispersions. The left panel discriminates bulge types by morphology, and the right panel discriminates them by their Sérsic index.

5.4. Velocity Dispersion Gradients

Inspection of the individual rotation curves reveals a wide variety of structures; however, in particular, the shape of the velocity dispersion profile seems to fall into two rough classes. In Figure 6 we show the kinematic profiles for the two galaxies NGC 3898 and NGC 4448 from our sample. Depicted are the velocity, the velocity dispersion, and the h_3 and h_4 moments of the Gauss–Hermite expansion of the LOSVDs. Dashed lines indicate the bulge radius from the photometric decomposition. While in the case of NGC 3898 the velocity dispersion rises all the way to the center, NGC 4448 has a relatively flat dispersion profile within the bulge radius.

Similarly to Fisher (1997) we examine, the logarithmic slope of the velocity dispersion within the bulge radius and call it γ. We derive the slope point-wise and then take the average, i.e.,

$$\gamma = \left\langle \frac{\Delta \log(\sigma)}{\Delta \log(r)} \right\rangle |_{r_{\rm min}<r<r_b}, \quad (5)$$

where $r_{\rm min}$ always excludes the inner FWHM of the seeing of the particular observation and in some cases is chosen larger to exclude central features like nuclear regions of enhanced star formation (see Appendix B). In Figure 6 we also overplot lines that correspond to the derived γ values. Further, in order to avoid a dependence of the slope on the particular binning scheme of each kinematic data set, we use a different binning for the purpose of determining γ: we bin radially in five equally sized bins in $\log(r)$. In cases where the resulting bins do not all contain at least one data point, we use our previous bins.

An alternative to the presented method is using the ratio of the averaged velocity dispersions within two annuli within the bulge radius

$$\delta = \frac{\langle \sigma \rangle |_{r_{\rm min}<r<r_b/3}}{\langle \sigma \rangle |_{r_b/3<r<r_b}} \quad (6)$$

as proxy for the slope. The choice of $r_b/3$ as cut radius for the two different annuli is somewhat arbitrary, but we do not find a strong dependence of our results on the specific radius chosen. Both values for the slope, γ and δ, are reported in Table 9.

We find that all bulges that are classified as pseudobulges indeed show flattened velocity dispersion profiles or even sigma drops (e.g., NGC 3351, NGC 3368, and NGC 3627 in Figure 16). The dispersion profiles of many pseudobulges are sometimes slightly asymmetric. On the other hand, a majority of the classical bulges show centrally peaked velocity dispersion

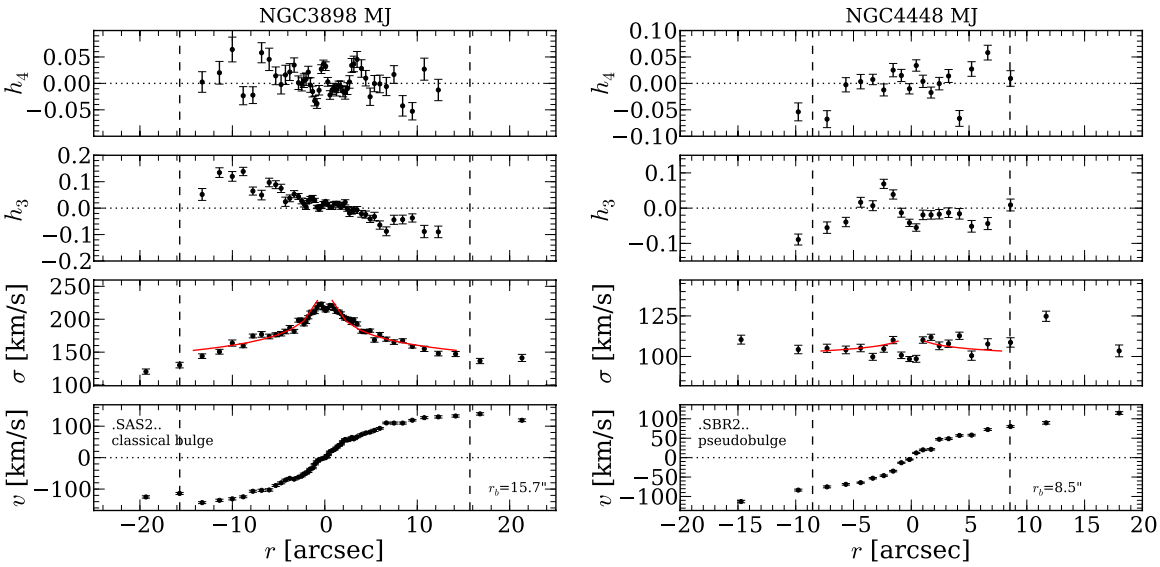

Figure 6. Major axis kinematic profiles for NGC 3898 and NGC 4448. Positive radii are east of the galaxy center. We plot from bottom to top the rotational velocity, velocity dispersion, and h_3 and h_4 moments. The curvature of the red lines correspond to the derived logarithmic slope of the dispersion profile; they are scaled to match the depicted profile. Their extent indicates the radial range which is taken into account for the derivation of the slope (see the text).

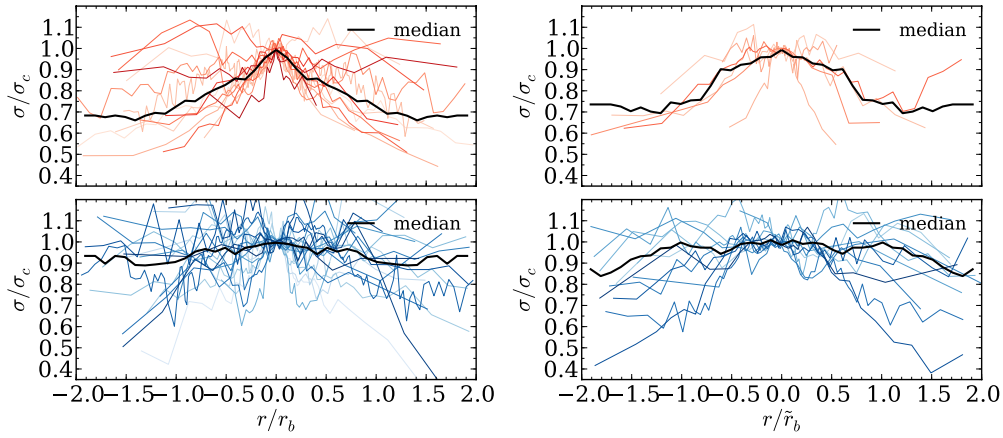

Figure 7. Major axis (left panels) and minor axis (right panels) velocity dispersion profiles, normalized by central velocity dispersion and bulge radius. Profiles of classical bulges are plotted in red in the respective upper panels, those of pseudobulges in blue in the corresponding lower panels. Different color shades correspond to different galaxies. The thick black line shows the median profile for all bulges in one panel. The bulge radii for the minor axis profiles have been corrected using the mean bulge ellipticity according to $\tilde{r}_b = (1 - \langle\epsilon\rangle) \cdot r_b$.

profiles (e.g., NGC 1023, NGC 2841, NGC 2880, and NGC 3245 in Figure 16).

Figure 7 summarizes this finding qualitatively, where we plot the velocity dispersion profiles along the major and minor axes for all our bulges separated by bulge type, and normalized by central dispersion and bulge radius. We do not plot bulges that were left unclassified. For this plot we adjust the bulge radius that was obtained from a major axis profile by the mean ellipticity in the bulge region. While not as clear, partly due to the lower number of profiles, but also probably partly due to the subtleties of choosing a correct radius for the normalization, we again find that classical bulges tend to show centrally rising velocity dispersions.

In Figure 8 we now plot the Sérsic index from the photometric decomposition as a function of both metrics for the slope of the velocity dispersion. Similar to the distributions of central velocity dispersion, there is significant overlap in profile slope. Nonetheless, the bulges with large values of Sérsic index tend to have steeply decaying dispersion profiles. Similarly, the bulges with low Sérsic indices more commonly have flat dispersion profiles. This result is true for both the logarithmic slope of dispersion and the dispersion ratio.

The increasing slope of velocity dispersion with Sérsic index is not fully unexpected. For instance, Ciotti (1991) describes a series of models for isotropic and spherical galaxies which have surface brightness profiles that follow a Sérsic law. He gives projected velocity dispersion profiles for his models. Outside of the very central regions ($r > r_e/10$), and for Sérsic indices larger than one, the slope is a monotonically increasing function of n. We calculate slopes and σ ratios for these profiles in a similar manner as we did for our data. One caveat of this exercise is that our definition of a bulge radius is not applicable in the case of the one-component models. Also, we have to choose an inner cut radius for the fit as the models feature central sigma drops in the case of small n. Sigma drops are an observed phenomenon (e.g., Falcón-Barroso et al. 2006), but our spatial resolution is typically not fine enough to resolve these. We somewhat arbitrarily fit for γ in the radial range of $r_e/10 < r < r_e$ and calculate σ ratios for $r_e/10 < r < r_e/3$ and $r_e/3 < r < r_e$. Note that our effective bulge radii are on average 15% smaller

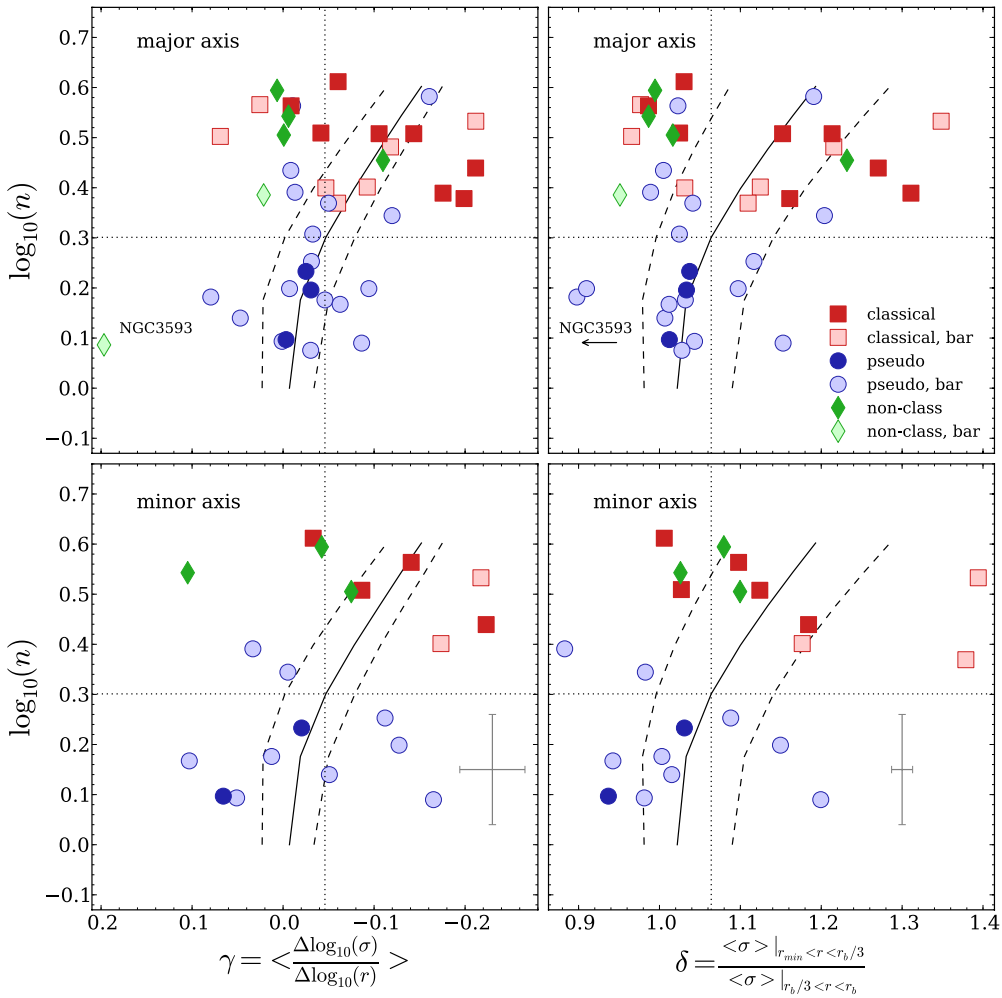

Figure 8. Sérsic index n is shown as a function of both metrics for the flatness of the velocity dispersion profile, γ and δ, respectively. Upper left: the major axis logarithmic slope of the velocity dispersion. Red squares and blue circles correspond to classical bulges and pseudobulges, respectively. Open symbols denote barred galaxies. The green diamonds represent unclassified objects. The black solid line shows the respective behavior of the isotropic models in Ciotti (1991); here the slopes were calculated in the radial range $r_e/10 < r < r_e$. The dashed lines show the γ values one would obtain by choosing the outer integration radius 50% smaller or larger. The horizontal line marks a Sérsic index of two. The vertical dotted lines mark $\gamma = -0.046$ and $\delta = 1.06$, the respective values that the isotropic models take for a Sérsic index of 2. Upper right: the ratio of the averaged velocity dispersion in two different annuli. NGC 3593 falls far to the left with $\delta = 0.7$ (see discussion in Section 6 and Appendix B). Lower panels: same for the minor axis dispersions. The radii were adjusted according the mean bulge ellipticity $\tilde{r}_b = (1 - \langle\epsilon\rangle) \cdot r_b$. The error bars correspond to the typical errors in the derived quantities, they also apply to the upper panels.

than the definition of the bulge radius that we use throughout the work. In Figure 8 we overplot the obtained values as a black line. The dashed lines show the range of values one would obtain by choosing 50% larger or smaller outer cut radii for the integration. While the spherical and isotropic galaxies are a very simplistic model for the variety of bulges in our sample, one can see that the general trends are reproduced; however, a more detailed dynamical modeling is needed to confirm this result.

In the major axis plots all unbarred pseudobulges fall below or very close to $\gamma = -0.05$ and $\delta = 1.06$ (the corresponding values of the isotropic models for $n = 2$) and only one unbarred classical bulge falls below $\gamma = -0.05$. However, 3 out of 8 unbarred classical bulges do fall significantly below $\delta = 1.09$ suggesting that γ is more successful in discriminating bulge types. Again this picture is complicated further once barred galaxies are taken into account. The additional component of a bar seems to lead toward flatter dispersion profiles.

5.5. Influence of Seeing on Velocity Dispersion

The seeing disk and the width of the slit will *smear* the observed velocities and can create increases in the observed LOSVD. This effect is commonly known as *slit smearing*. All data presented here were observed with a slit width of 1″. The effect of slit smearing on the velocity dispersion is therefore expected to be negligible compared to the effect caused by the seeing (>1.2″ in all cases). At least two galaxies, NGC 3384 and NGC 3521, do show peaks in velocity dispersion in the central arcseconds (see Figure 16). In both galaxies the velocity profile also rises rapidly in the center. We test whether this rapid rise in combination with the seeing may be responsible for the observed dispersion peak. We model the PSF with a Gaussian of the same FWHM. We then calculate the standard deviation of the velocity which is weighted by the PSF amplitude at all radii and subtract the result from the observed velocity dispersion. In this simple one-dimensional model the PSF smearing does generate a central peak which is of similar size and amplitude as the observed one. We cannot rule out the possibility that the central peaks of NGC 3384 and NGC 3521 can be explained through PSF-smearing alone. We however refrain from correcting the presented velocity dispersions as an accurate correction has to include the knowledge of a high-resolution luminosity profile and a more rigorous,

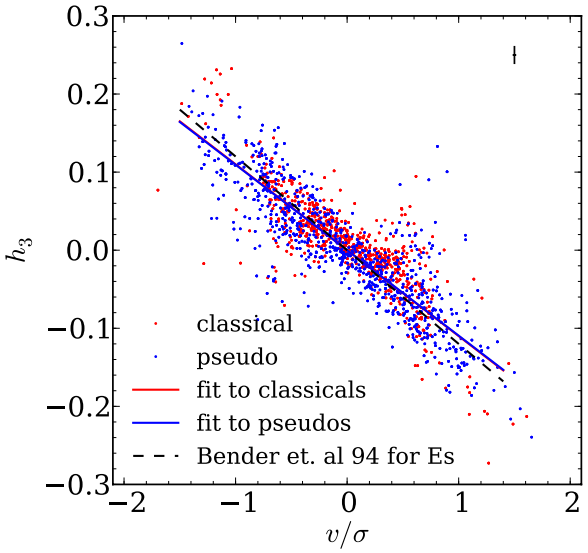

Figure 9. Local anti-correlation between h_3 and v/σ along the major axis for the galaxies in our sample. We only plot points for which the error in h_3 is lower than 0.05. Plotted are all galaxies for which the bulge was classified either as classical (red) or a pseudobulge (blue). Typical error bars are shown in the upper right of the diagram. The red and blue lines correspond to the fitted linear correlations for the classical and pseudobulges, respectively. The dashed black line represents the value for the correlation that Bender et al. (1994) obtained for their sample of early types.

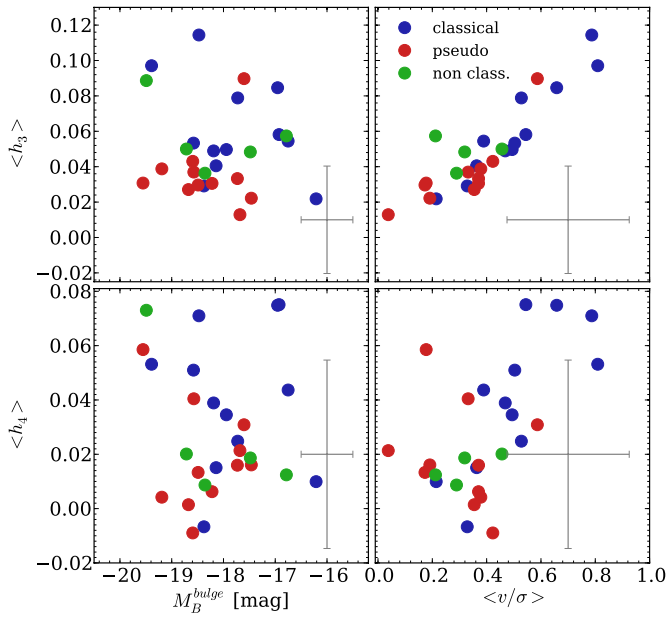

Figure 10. Major axis correlations between bulge-averaged Gauss–Hermite moments $\langle h_3\rangle$ and $\langle h_4\rangle$, bulge luminosities, and $\langle v/\sigma\rangle$. Upper left: $\langle h_3\rangle$ as function of bulge H-band magnitude. Red circles represent classical bulges, blue circles are pseudobulges, green circles represent unclassified bulges. Upper right: $\langle h_3\rangle$ as function of $\langle v/\sigma\rangle$. No inclination corrections were applied. Lower left: $\langle h_4\rangle$ as function of bulge magnitude. Lower right: $\langle h_4\rangle$ as function of $\langle v/\sigma\rangle$. Representative error bars are displayed in the lower right hand part of each panel. In the case of the bulge magnitude they correspond to the typical error. For all other plotted quantities the larger error bars correspond to the typical rms scatter of that quantity within the considered radial range, whereas the smaller error bar corresponds to the formal error of the derived average.

two-dimensional modeling of the PSF. We rather exclude the central peaks from the further analysis.

5.6. Distribution of h_3 and h_4 Moments

As h_3 measures the asymmetric deviation from a purely Gaussian distribution it detects lower velocity tails of the velocity distribution along the line of sight. Such tails arise naturally in disks (Binney & Tremaine 1987). Bender et al. (1994) found that local h_3 and local v/σ are strongly anti-correlated with a slope of -0.12 in their sample of elliptical galaxies. Fisher (1997) finds a similar anti-correlation in the inner regions of his lenticular galaxies but also sees that, for a number of his objects, at values of $v/\sigma \approx 1$ the anti-correlation turns, at least briefly but abruptly, into a correlation.

We reproduce the plot for the local correlation of h_3 and v/σ from Bender et al. (1994) for our sample in Figure 9 and color-code pseudobulges in blue and classical bulges in red. We find that the same correlation is reproduced in our intermediate-type galaxies. The h_3 moments are generally anti-correlated with v/σ out to $v/\sigma \approx 0.5$, irrespective of bulge type. A linear fit to the complete set of data points gives a slope of $(h_3 = (-0.106 \pm 0.001) \cdot v/\sigma)$. Separate fits to the subsample of classical bulges and pseudobulges give values that are indistinguishable within the errors. A Kolmogorov–Smirnov test (Smirnov 1939; Press 2002) for the median values of $v \cdot \sigma^{-1} \cdot h_3^{-1}$ within individual galaxies yields a probability of 76% for the hypothesis that the classical and the pseudobulges stem from the same distribution. This local correlation is reproduced in the mean values for the bulge region (Figure 10).

We further test for a possible correlation with H-band bulge magnitude (see Figure 10) and the bulge-averaged value $\langle h_3\rangle$. We do not see any correlation between bulge luminosity and $\langle h_3\rangle$.

The h_4 moment of the Gauss–Hermite expansion measures the symmetric deviation from a Gaussian distribution. Negative h_4 describe a more boxy, centrally flattened distribution, more positive values describe centrally peaked distributions with extended wings. The averaged h_4 moments in the bulges are generally close to zero, the median for the complete sample of major axis spectra is 0.03 with a standard deviation of 0.046. None of our bulges show obvious dips in the h_4 profile like the ones described by Debattista et al. (2005) and Méndez-Abreu et al. (2008), but this diagnostic for boxy peanut-shaped bulges only applies to low inclinations ($i < 30°$), given that the inclinations of most of our galaxies are larger than 30° (41 out of 45) this is not surprising. However, 14 galaxies show a double peak in the h_4 profile within the bulge region (e.g., NGC 1023, NGC 3031, NGC 3945, and NGC 7331 in Figure 16). This is typically seen in combination with a rapid increase of the rotational velocity and relatively strong h_3 moments. From our Monte Carlo simulations described in Section 4.1 we can rule out that the observed peaks are a result of a degeneracy between h_3 and h_4 moments in the fit.

We find no correlation between the averaged $\langle h_4\rangle$ moments and the bulge luminosities. However, while the error bars are large, larger h_4 moments seem to be found in bulges with larger averaged v/σ (Figure 10). Bender et al. (1994) also discuss the possibility of a similar trend in their subsample of rotationally flattened galaxies.

There is a mild indication that pseudobulges and classical bulges show different distributions in the average $\langle h_3\rangle$ and $\langle h_4\rangle$ moments. For pseudobulges we find an average value for $\langle h_3\rangle$ of 0.06 with an rms scatter of 0.03 while for classical bulges the mean value of $\langle h_3\rangle$ is 0.04 with a scatter or 0.03. A K-S test and a Student's two-tailed t-test for two independent samples yield a probability of 0.3% and 3%, respectively, for the two subsamples to stem from the same distribution. For $\langle h_4\rangle$ we find and average

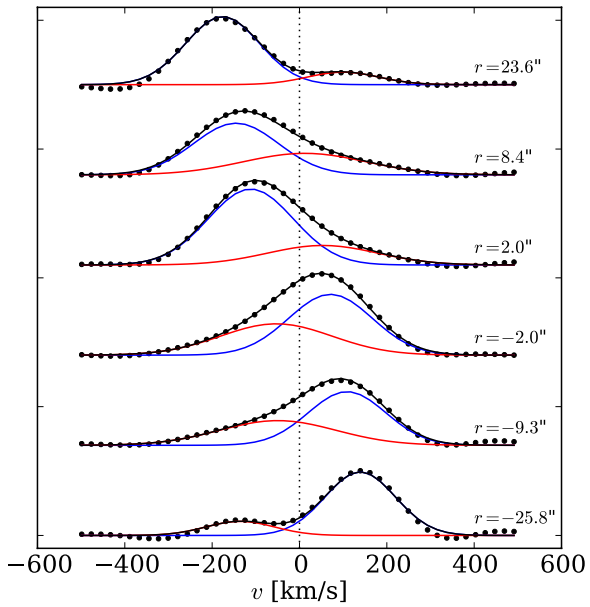

Figure 11. Example for the double-Gaussian decompositions for NGC 3521. The FCQ derived full line-of-sight velocity distribution for five selected radii is plotted in black. The two-Gaussian kinematic decompositions plotted in red and blue.

(A color version of this figure is available in the online journal.)

of 0.04 with a scatter of 0.02 in the pseudobulges, and 0.02 with a scatter of 0.02 in the classical bulges. Here the K-S test finds a 5% probability for the null hypothesis while the *t*-test yields a 1.5% probability. As both the h_3 and the h_4 moment are affected by the inclination and the scatter is large, this trend has to be taken with caution. A larger sample and kinematic modeling will be needed to confirm if this is a signature of systematic different anisotropies in the two classes of bulges.

5.7. Extreme Moments and Multiple Kinematic Components

Five galaxies show extreme h_3 and h_4 moments. The most extreme case, NGC 3521, (a classical bulge) exhibits values of h_3 and h_4 as large as 0.24 and 0.35, respectively (see Figure 16). NGC 3945, NGC 4736, NGC 7217 (all pseudobulges), and NGC 7331 (unclassified) show values of h_3 and h_4 of up to 0.2. The LOSVD is poorly reproduced by a Gauss–Hermite expansion at the radii of such extreme higher moment values (see Figure 11). The reason lies in the existence of a secondary kinematic component in all those cases. For NGC 3521 this has been reported by Zeilinger et al. (2001) who attributed the counter-rotating stellar component to the presence of a bar. The two-component nature of NGC 7217 was discovered before by Merrifield & Kuijken (1994). They suggest that the second component is the result of an extended period of accretion with intermittent change of angular momentum of the infalling material. Prada et al. (1996) reported a counter-rotating bulge in NGC 7331.

Two more systems in our sample, NGC 2841 (Bertola & Corsini 1999) and NGC 3593 (Bertola et al. 1996), were reported to host counter-rotating components, and a kinematically decoupled component was found in NGC 4698 (Corsini et al. 1999; Bertola et al. 1999; Falcón-Barroso et al. 2006) see Pizzella et al. (2004) for a review. NGC 3593 is the only galaxy in our sample for which the rotation curve itself already reveals counter-rotation through a twist—the rotation changes sign with respect to the systemic velocity at a radius of about 20″ (see Figure 16 and Appendix B). The case is similar although not as pronounced for NGC 4698 where the rotation curve becomes very flat toward the center (see Figure 16). However, in these cases the secondary component does not result in unusually strong h_3 and h_4 moments in our data.

Table 10
Light Fractions in Kinematic Subcomponents

Galaxy	Morph.	Disk Light (%)	Light in Fast Component (%)
(1)	(2)	(3)	(4)
NGC 3521	SAB(rs)bc	34	44
NGC 3945	(R)SB$^+$(rs)	2	34
NGC 4736	(R)SA(r)ab	55	50
NGC 7217	(R)SA(r)ab	55	38
NGC 7331	SA(s)b	26	47

Notes. Comparison of the amount of light in the lower dispersion component to the light that one would expect from the photometric decomposition. We integrate the amplitudes of the Gaussian fits to the two components over all radii shown in Figure 12. (1) Galaxy. (2) Morphology (RC3). (3) Integrated light in the disk component from the extrapolation of the outer disk exponential profile. (4) Integrated light in the lower dispersion component.

In an attempt to make a fairer treatment of their complexity, we decompose the FCQ-derived LOSVDs into two separate Gaussian components in a similar manner to Scorza & Bender (1995) and Zeilinger et al. (2001). We use the Metropolis–Hastings algorithm (Hastings 1970; Press et al. 2007) to infer the parameters and error bars. Before the fit, the spectra are binned to a minimum S/N of 75 pixel^{-1}. We run four simultaneous chains for each radial bin. The step width is tuned to achieve a 25% acceptance ratio and after convergence the first half of the chain is discarded (clipped). The run is aborted if the chains do not converge after 100.000 steps.

Figure 12 shows the result of this decomposition. The plotted values are the maximum-likelihood values, and the end of the error bars mark the 20% and 80% quantiles in all four chains after clipping. Central values with strong degeneracies between the parameter sets are omitted. In all five galaxies we do find significant second components under the assumption that individual components are purely Gaussian. In Table 10 we list the integrated fractions of light in the two different kinematic components and compare those to the values that one would expect from the photometric decomposition.

6. DISCUSSION

6.1. Dichotomous Dispersion Profiles of Classical Bulges and Pseudobulges

It is commonly assumed that the bulge light—typically determined from a bulge-disk decomposition—represents a dynamically hot component, yet it has been known for a long time that rotation-supported bulges exist (Kormendy 1982). Also, many bulges have lower central velocity dispersions than expected from the Faber & Jackson (1976) relation (Kormendy & Kennicutt 2004). Falcón-Barroso et al. (2006); Ganda et al. (2006) find that several galaxies in the SAURON survey have centers that are dynamically colder than the surrounding disks. Thus, it is now clear that not all galaxies fit the picture that a bulge is a dynamically hot component.

There is an observed dichotomy in bulge properties including Sérsic index, bulge morphology, star formation and ISM properties, and optical color (Carollo et al. 1997; Gadotti & dos Anjos 2001; Kormendy & Kennicutt 2004; Fisher 2006; Fisher

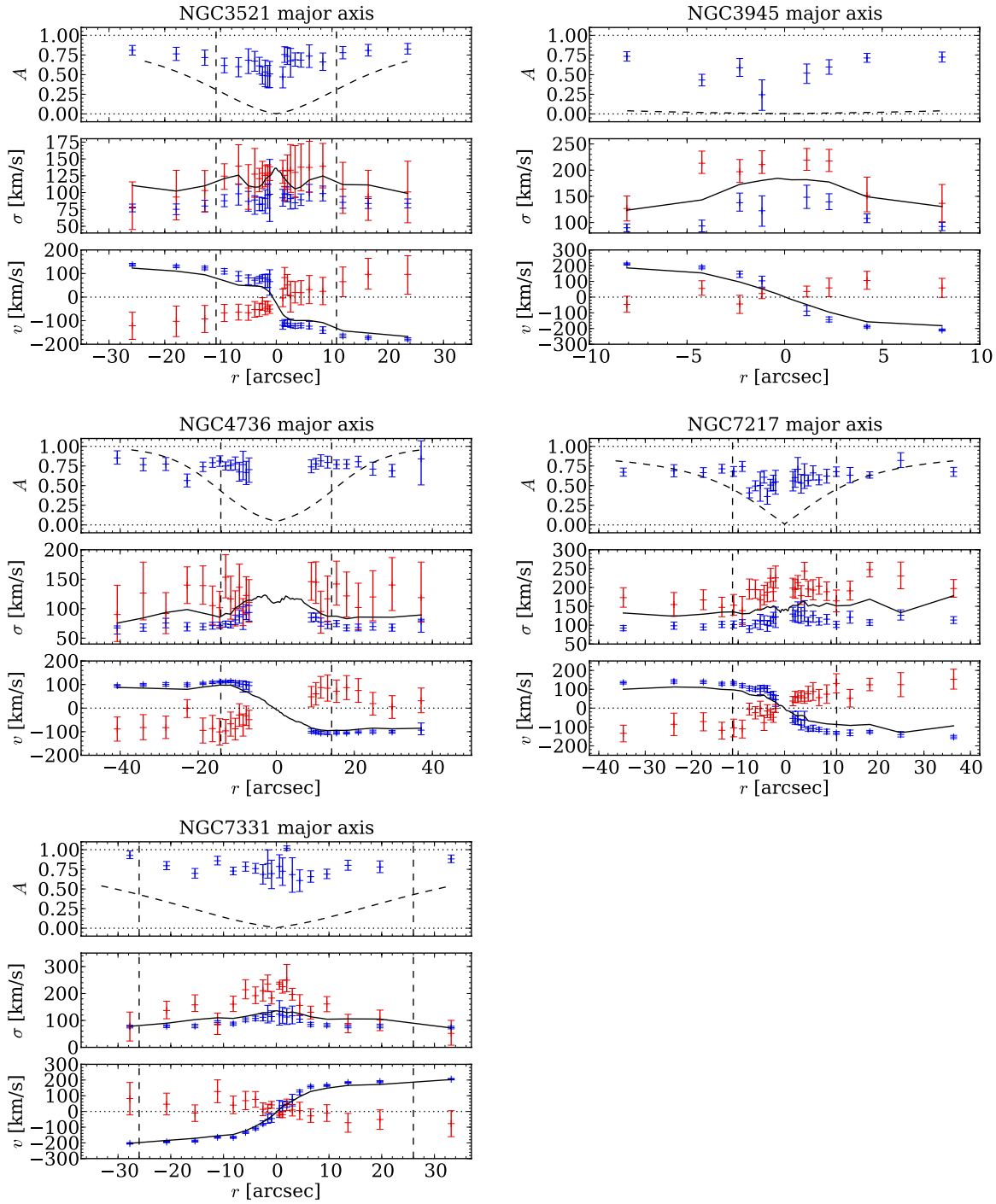

Figure 12. Kinematic decompositions of the major axis data of NGC 3521, NGC 3945, NGC 4736, NGC 7217, and NGC 7331. In a procedure similar to Scorza & Bender (1995) and Zeilinger et al. (2001) we fit two Gaussians to the FCQ derived full LOSVDs at all radii. Blue and red error bars show the mean velocity and dispersion of the two Gaussians where the Metropolis–Hastings algorithm chains achieved convergence. The length of the error bars represent the 20% and 80% quantiles. Black curves indicate the FCQ-fitted moments of a single Gauss–Hermite expansion of the LOSVD. Here the error bars are comparable to the thickness of the line. The upper panel shows the relative weight of the fast component with respect to the total light. The dashed curve shows the disk to total ratio from the photometric decomposition. Vertical lines indicate the bulge radius.

& Drory 2008, 2010). Recently, Fisher & Drory (2010) showed that the dichotomous properties in Sérsic index, morphology, and ISM properties are consistent. Furthermore they showed that bulges of different type occupy different regions in the projection of fundamental plane properties, thus indicating that there are very likely two physically distinct classes of bulges. Are dynamics part of this dichotomy?

The high spectral resolution of 39 km s^{-1} of our data, enables us to recover dispersions out into the disk regions in many of our targets—a feature uncommon to many similar surveys. We extract LOSVDs using the FCQ algorithm with additional procedures to account for nebular emission and template mismatch. We recover v, σ, h_3, and h_4 moments of a Gauss–Hermite model of the LOSVDs as function of radius.

We observe a great variety of shapes of kinematic profiles (see Figure 16 and their detailed description in Appendix B). Similarly to Falcón-Barroso et al. (2006) and Ganda et al. (2006), we find that it is not necessarily true that the center of a bulge has the highest observed velocity dispersion (e.g., NGC 3593). In our sample only ∼1/3 of the galaxies have centrally peaked velocity dispersion profiles (like NGC 3898). Many galaxies have roughly flat velocity dispersion profiles. In these galaxies there is no apparent transition in velocity dispersion from the bulge to the disk region unlike in the stellar surface brightness profile (e.g., NGC 4448 and NGC 5055).

It is interesting to note that to the radial extent of our data, in many of these cases the disk velocity dispersion is as high as the central velocity dispersion of the galaxy. For example in NGC 4448 the disk velocity dispersion remains above 100 km s^{-1}. Therefore some disks of spiral galaxies are not necessarily cold stellar systems over the radii that we cover in this study.

From minor axis data of 19 S0 to Sbc bulges, Falcón-Barroso et al. (2003) showed that higher ellipticity bulges have shallower velocity dispersion profiles. If pseudobulges appear photometrically flattened then one might expect that the steepness of the dispersion profile should correlate with bulge type. We show in Figure 7 that the shape of the velocity dispersion profile correlates very well with bulge type. Galaxies with classical bulges have centrally peaked profiles. Galaxies with pseudobulges have, on average, flat dispersion profiles. We have attempted to quantify this using the logarithmic derivative of the velocity dispersion as function of radius (Equation (5)) and also the ratio of dispersions at different radii (Equation (6)). We find that pseudobulges and classical bulges occupy different regions in the parameter space of logarithmic derivative of velocity dispersion and Sérsic index (see Figure 8) in a way that is not inconsistent with models of dynamically isotropic systems (Ciotti 1991).

It is important to note that the dynamics of a few galaxies are not well described by a simple monotonic trend of velocity dispersion with radius; we stress that for the purpose of this paper we are interested in the bulk properties of the distribution of stellar dynamics. The great variety of shapes in dispersion profiles that we observe (for a detailed description, see Appendix B) is likely to be a consequence of the fact that there are multiple ways to heat galactic disks, for example through mergers (van Albada 1982; Quinn et al. 1993; Eliche-Moral et al. 2006; Hopkins et al. 2008), bars (Saha et al. 2010), and other disk instabilities (Sellwood & Wilkinson 1993; Combes et al. 1990). Even under the strong assumption that classical bulges and pseudobulges are dynamically distinct, it does not seem plausible that any simple description of the kinematic profile cleanly separates classical from pseudobulges.

A few classical bulges in barred galaxies such as NGC 3992 do not seem to fit this general picture. However, all those galaxies are barred and it is conceivable that bars may distort the kinematic profile of a classical bulge as they vertically heat the disk they reside in (Gadotti & de Souza 2005; Saha et al. 2010). Central velocity dispersions lie higher by a factor of two than at the bulge radius in the most extreme cases in our sample, e.g., in NGC 1023, NGC 3898, and NGC 4203. If bars raise velocity dispersions by a factor of up to four as suggested by Saha et al. (2010), the signature of a central dispersion peak can of course be easily washed out.

NGC 4826 has extreme amounts of dust in its central region—hence its name "black eye" or "evil eye" galaxy. The bulge was consequently classified as a pseudobulge by Fisher & Drory (2008). It stands out, however, as it has a relatively high Sérsic index of 3.9 ± 0.88 for a pseudobulge. The *V*-band value of $n = 3.94 \pm 0.68$ (Fisher & Drory 2008) agrees well. The bulge radius of 25.4″ seems small once the kinematic data are taken into account. The velocity dispersion starts rising at about 50″, which corresponds to the radius of the final flattening of the rotation curve. It is conceivable that the large amount of dust in its center, which is easily also visible in the infrared, may affect the decomposition. If one was to take the value of 50″ as the bulge radius then the γ value would become −0.33 (0.01 before) and the sigma ratio would take a value of 1.29 (1.08 before). This would move NGC 4826 significantly further to the right in both plots, into the region occupied by classical bulges, in much better agreement with the Sérsic index. Further, the disk of NGC 4826 is relatively free of dust and actually resembles an S0. We hypothesize that the unusual morphology is a result of a recent merging event. A satellite may have fallen into an S0-like disk and brought in dust and triggered star formation. This hypothesis is supported by the existence of two counter-rotating gaseous disks observed by Braun et al. (1992, 1994). We labeled NGC 4826 as non-classified throughout this work. NGC 3593 has a very large value of γ and a very small sigma ratio, i.e., it falls far to the left in both diagrams. This is a result of the strong depression in velocity dispersion in the bulge region. NGC 3593 is the only galaxy in the sample where we observe actual counter-rotation in the sense of a change of sign of the mean rotational velocity in the bulge region. The small Sérsic index of 0.81 supports the picture that the bulge region is dominated by a kinematically cold and distinct but luminous disk (Bertola et al. 1996). NGC 2681 is classified as a pseudobulge by morphology and yet has a relatively large Sérsic index of $n = 3.8$. Further, it has a centrally peaked dispersion profile with $\gamma = -0.16$ and $\delta = 1.19$. This agreement of photometric structure and dispersion slope prompts us to reassess the morphological classification. While the disk shows relatively little amounts of dust, a high contrast dust spiral within in the bulge easily seen in *HST* F555W, offers a clear sense of rotation. Also the spiral is not obviously misaligned with the outer disk. This galaxy may represent a prototypical case for the breakdown of the morphological classification scheme. However, it shows multiple bars—possibly three (Erwin & Sparke 1999)—and hence the central heating may also be a consequence of its complicated dynamical structure. NGC 3521 has a seemingly a relatively flat dispersion slope with values of $\gamma = -0.01$ and $\delta = 0.99$. We discuss this object at the end of the next section.

6.2. Rotational Support

In order to study the level of rotational support of a stellar system, it has become common practice to study its location in the $v_{\rm max}/\langle\sigma\rangle$ versus ϵ diagram (Illingworth 1977; Binney & Tremaine 1987; Kormendy 1993)—where $v_{\rm max}$ measures the maximum rotational velocity and $\langle\sigma\rangle$ the averaged velocity dispersion within a certain radius, and ϵ the system's ellipticity. One can also directly compare $v_{\rm max}/\langle\sigma\rangle$ to the expected values of an oblate-spheroidal system with isotropic velocity dispersion. For instance, Kormendy & Illingworth (1982) define the anisotropy parameter $(v/\sigma)^* = (v_{\rm max}/\langle\sigma\rangle)/\sqrt{\epsilon/(1-\epsilon)}$ as a measure for the rotational support of a stellar system. Values of $(v/\sigma)^* \approx 1$ point toward a support by rotation whereas values <1 indicate support by anisotropy. Those measures involve the ellipticity of the system which is typically subject to

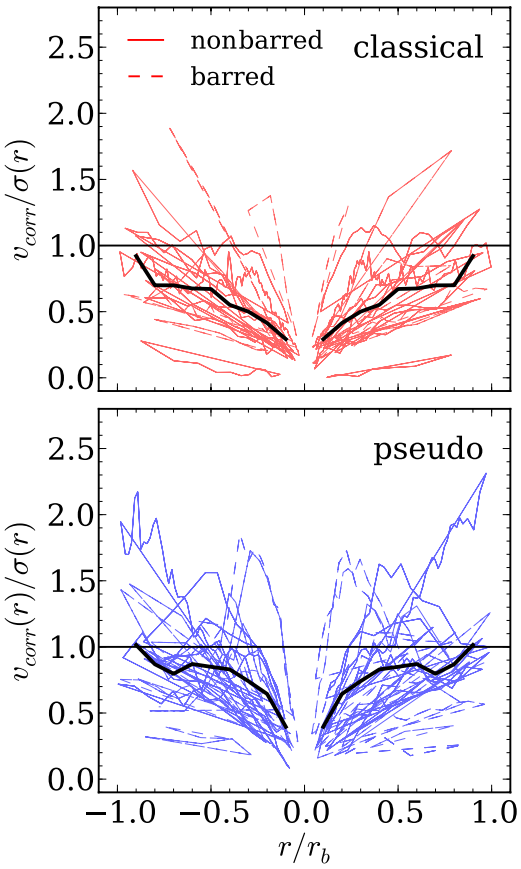

Figure 13. Local $(v_{\rm corr}/\sigma)(r)$ along the major axis, the radii are normalized by bulge radius. The velocities are corrected for inclination through $1/\sin(i)$. Classical bulges are plotted in the upper panel, and pseudobulges in the lower panel. The solid black line marks the median of all profiles.

(A color version of this figure is available in the online journal.)

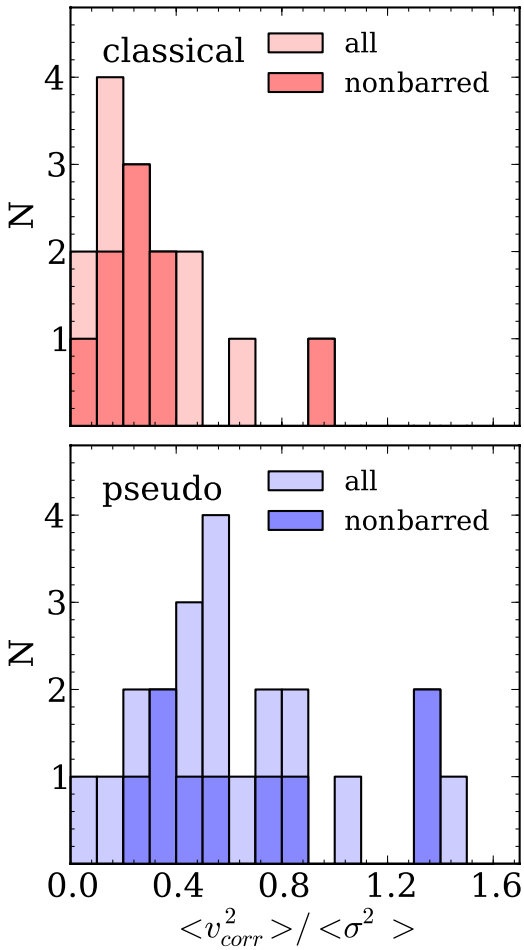

Figure 14. Histograms for the averaged values of $\langle v^2\rangle/\langle\sigma^2\rangle$ (Binney 2005). The velocities are corrected for inclination through $1/\sin(i)$. Classical bulges are plotted in the upper panels, and pseudobulges in the lower panels.

(A color version of this figure is available in the online journal.)

relatively large uncertainties, especially when measured for galaxies which are dominated by large quantities of dust. Here, we decide to rather examine the local $(v_{\rm corr}/\sigma)(r)$, i.e., as a function of radius, and the averaged values of $\langle {v_{\rm corr}}^2\rangle/\langle\sigma^2\rangle$ (Binney 2005) across the bulge region, $v_{\rm corr} = v_{\rm obs}/\sin(i)$ is the inclination corrected velocity at a given radius. We use inclinations from Hyperleda (see Table 1). We apply no further correction to the velocity dispersion.

In Figure 13 we plot $(v_{\rm corr}/\sigma)(r)$ separately for classical and pseudobulges. We further plot histograms of the bulge-averaged quantities in Figure 14. Again we normalize the radii by the bulge radius and exclude the central seeing FWHM from the analysis. While there is significant overlap between the two subsamples, pseudobulges are biased toward larger $(v_{\rm corr}/\sigma)(r)$. This is especially seen in the histograms for the averaged values. A Kolmogorov–Smirnov test (Smirnov 1939; Press 2002) yields a probability of 0.8% (1.9%) for the classical and the pseudobulges in the full (nonbarred) sample to stem from the same distribution. A Student's two-tailed *t*-test for two independent samples yields a probability of 0.7% (2.5%) for the classical and the pseudobulges in the full (nonbarred) sample. This result supports a picture of increased rotational support of pseudobulges that was originally described by Kormendy (1993) and discussed in detail in Kormendy & Kennicutt (2004), see also Kormendy & Fisher (2008).

While the average values of γ and $\langle v^2\rangle/\langle\sigma^2\rangle$ are different for classical and pseudobulges, neither of the two quantities separates the bulge types. In Figure 15 we combine both and plot $\langle v^2\rangle/\langle\sigma^2\rangle$ against the logarithmic slope of the velocity dispersion, γ, for the bulges in our sample. In the left panel we discriminate bulges morphologically and in the right based on the bulge Sérsic index. The dashed line is drawn to contain all the pseudobulges. Classical bulges both tend to have low $\langle v^2\rangle/\langle\sigma^2\rangle$ and steeper negative slopes than pseudobulges.

There are several galaxies with large Sérsic index that fall dynamically into the region of pseudobulges. We have discussed the possibility that bars mask or destroy the kinematic signature of a classical bulge. However, two nonbarred high-Sérsic index galaxies remain (NGC 3521 and NGC 7331; NGC 3521 also has classical bulge morphology). Both galaxies have centrally peaking velocity dispersion profiles but they also show a rise in velocity dispersion at larger radii (see Appendix A), yet still within the radius of the bulge. This is also a feature that is prominently seen in the dispersion profile of NGC 3031, but in this case the effect on the position in the $\langle v^2\rangle/\langle\sigma^2\rangle$ versus γ plane is not as dramatic. This behavior is not what we observe in pseudobulges, which have flat dispersion profiles. None of these three galaxies violate the general dichotomy observed in Figure 7. Therefore it is likely that their outlier location is due to a failure in the machinery of measuring dynamical quantities. NGC 7331 and NGC 3521 both show signs of counter-rotating components and NGC 3031 is well known to be interacting.

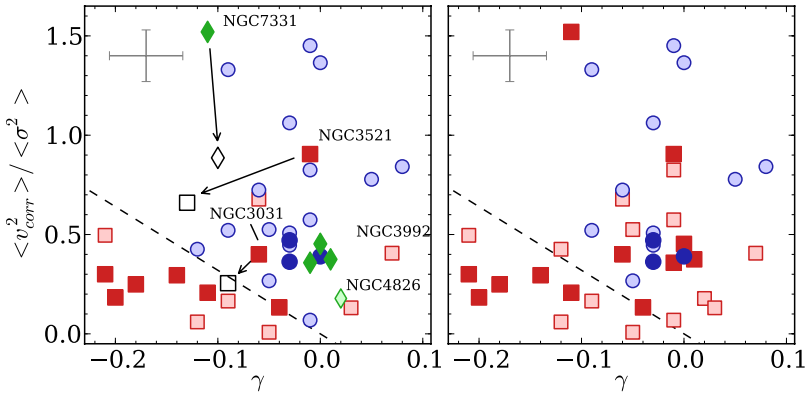

Figure 15. Bulge-averaged quantity $\langle v^2\rangle/\langle\sigma^2\rangle$ as function of the slope of the velocity dispersion, γ. In the left panel we discriminate bulge types based on morphology. Pseudobulges are colored blue, classical bulges red, and bulges that we do not classify are colored green. Light-shaded symbols represent barred galaxies or galaxies hosting an oval. In the right panel we discriminate by Sérsic index (blue $n \leqslant 2.1$, red otherwise). For NGC 3521, NGC 3031, and NGC 7331 we remeasure γ changing the outer radius cut to isolate only the central dispersion peak as described in the text. The corresponding new locations are marked as black open symbols. The dashed line is drawn to contain all the pseudobulges.

It is possible in each of these galaxies that an outside mechanism is superimposing extra kinematic structure that is visible as an outside rise in the velocity dispersion profile of the bulge. We remeasure γ changing the outer radius cut isolating only the central dispersion peak. In the case of NGC 3031 this moves the measured dynamical quantities into the region of parameter space that is only occupied by classical bulges; both NGC 3521 and NGC 7331 move significantly closer.

Figure 15 illustrates agreement between kinematic diagnostics of the bulge dichotomy with structural and morphological indicators of bulge types.

6.3. Multiple Kinematic Components

We observe counter-rotation seen as secondary components in the full shape of the LOSVD in five systems (NGC 3521, NGC 3945, NGC 4736, NGC 7217, and NGC 7331; see Section 5.7). It is striking how clearly the LOSVDs can be decomposed into a low-dispersion and a high-dispersion component in all these cases. It is tempting to interpret the latter as the bulge and the former as the disk. However, if we plot the local disk-to-total ratios as obtained from the photometric decomposition over the values obtained from the kinematic decomposition (upper panels of Figure 12), then we see that the disk contribution from the photometry falls short in all cases. Therefore, the observed low-dispersion component within the bulge region is not simply the extension of the outer disk as more light contributes to this component as one would expect from the extrapolation of the outer disk exponential profile alone. It is important to point out that a Gauss–Hermite distribution with moderate h_3 moments can be modeled rather well by two individual Gaussians. h_3 moments, though, occur naturally in disks (Binney & Tremaine 1987) and are not a signature of an actual second component. Only in cases where the second component is clearly seen as a second peak in the LOSVD it is safe to assume that actually two distinct components contribute.

The observation of a counter-rotating component is very interesting in the light of the findings of Eliche-Moral et al. (2011). They use collisionless *N*-body simulations to study the characteristics of inner components such as inner disks and inner rings that were formed though a minor merger. For this, they simulate a number of mergers with different mass ratios and orbits. In general, while all their mergers formed an inner component supported by rotation, none of their mergers produced a significant bar. In their simulations all mergers with satellites on retrograde orbits do form a counter-rotating component while none of them leads to actual counter-rotation in the sense of a change of sign of the mean rotational velocity. A central increase of velocity dispersion and strong h_3 and h_4 moments are observed in a majority of their models. They further find, however, that v/σ and h_3 are generally anti-correlated within the inner components throughout all of their simulations. We see all these features reflected in the aforementioned galaxies. Of particular interest to us is the double peak in h_4 that their model *M6P1Rb* produced. Such double peaks are very pronounced in NGC 3945 and NGC 4736, but are also visible in the case of NGC 3521 and NGC 7331. In our small sample, three out of the five systems for which counter-rotation is observed are not barred; we think that a merging event is a likely formation scenario.

7. SUMMARY

In this paper we present kinematic profiles for the major axis of 45 intermediate-type (S0–Scd) galaxies. Our survey differs from other similar surveys in that we are able to resolve lower velocity dispersions which allows us to study kinematic features in cold systems like disks and pseudobulges. We combine these data with bulge-to-disk decompositions of the stellar light.

We find that bulges that have increased rotational support, as measured by larger values of $\langle v^2\rangle/\langle\sigma^2\rangle$, are likely to have lower Sérsic indices and show disk-like morphology.

Classical bulges on average tend to have higher central velocity dispersions than pseudobulges. In our sample the lowest central velocity dispersion in a galaxy with evidence for a classical bulge through a Sérsic index of 3.7 is $\sigma_{r_e/10} = 85 \pm 2$ km s^{-1} (NGC 7743).

We observe—for the first time—a systematic agreement between the shape of the velocity dispersion profile and the bulge type as indicated by the Sérsic index. Classical bulges have centrally peaked velocity dispersion profiles while pseudobulges in general have flat dispersion profiles and even at times show drops in the central velocity dispersion. We confirm that this correlation holds true if visual morphology is used for the bulge classification instead of the Sérsic index, as it is expected from the good correlation between bulge morphology and Sérsic index (Fisher & Drory 2010).

We observe that the disk regions of some of our galaxies have not always a low velocity dispersion. In some galaxies

the velocity dispersion remains above 100 km s^{-1} well into the region where the disk dominates the light.

We confirm the previously described multicomponent nature of the full LOSVD in NGC 3521 (Zeilinger et al. 2001), NGC 7217 (Merrifield & Kuijken 1994), and NGC 7331 (Prada et al. 1996) and find two additional systems—namely NGC 3945 and NGC 4736—with signatures of multiple kinematic components. They become apparent through a secondary peak or pronounced shoulder in the full LOSVD. We present double-Gaussian decompositions which show the presence of a counter-rotating stellar component in all these systems.

As in elliptical galaxies (Bender et al. 1994), we find a correlation of h_3 and v/σ, both locally as well as in the bulge-averaged quantities. We observe no correlation of the higher moments with bulge luminosity, however, we find a weak correlation between the average values of h_4 and v/σ.

Through examination of the figures in Appendix A it is clear that the kinematic profiles of bulge-disk galaxies commonly contain substructure. Furthermore nonaxisymmetric features in the stellar structure such a bars make understanding the kinematics of these galaxies more difficult. Future progress will require two-dimensional methods capable of resolving low velocity dispersions commonly found in pseudobulges. We are currently executing such a survey using the VIRUS-W spectrograph (Fabricius et al. 2008).

We thank Luca Ciotti for providing velocity dispersion profiles for the isotropic models presented in his 1991 paper. We thank Jesus Falcon Barroso of the SAURON collaboration who made kinematic maps of a number of the galaxies available to us in various formats which allowed for a detailed comparison of our data. We also acknowledge the help of Gaelle Dumas who provided SAURON data from her 2007 paper. We thank Peter Erwin for many fruitful discussions and his valuable comments. We also express our gratefulness to the efforts of the observing staff at the Hobby–Eberly Telescope (HET). Over the years of the duration of this survey they have constantly provided high-quality data, given very valuable background information, and have always been very helpful and approachable concerning technical aspects of the data. The HET is a joint project of the University of Texas at Austin, the Pennsylvania State University, Stanford University, Ludwig-Maximilians-Universitaet Muenchen, and Georg-August-Universitaet Goettingen. The HET is named in honor of its principal benefactors, William P. Hobby and Robert E. Eberly. The Marcario Low Resolution Spectrograph is named for Mike Marcario of High Lonesome Optics who fabricated several optics for the instrument but died before its completion. The LRS is a joint project of the HET partnership and the Instituto de Astronomia de la Universidad Nacional Autonoma de Mexico. The grism E2 used for these observations has been bought through the DFG grant BE1091/9-1. This work was supported by the SFB-Transregio 33 The Dark Universe by the Deutsche Forschungsgemeinschaft (DFG). This research has made use of the NASA/IPAC Extragalactic Database (NED) which is operated by the Jet Propulsion Laboratory, California Institute of Technology, under contract with the National Aeronautics and Space Administration. Some/all of the data presented in this paper were obtained from the Multimission Archive at the Space Telescope Science Institute (MAST). STScI is operated by the Association of Universities for Research in Astronomy, Inc., under NASA contract NAS5-26555. Support for MAST for non-*HST* data is provided by the NASA Office of Space Science via grant NAG5-7584 and by other grants and contracts. We acknowledge the usage of the HyperLeda database (http://leda.univ-lyon1.fr; Paturel et al. 2003). This publication makes use of data products from the Two Micron All Sky Survey, which is a joint project of the University of Massachusetts and the Infrared Processing and Analysis Center/California Institute of Technology, funded by the National Aeronautics and Space Administration and the National Science Foundation. This work is based, in part, on observations made with the *Spitzer Space Telescope*, which is operated by the Jet Propulsion Laboratory, California Institute of Technology under a contract with NASA. Finally, we thank the anonymous referee for the careful reading and the provided input that helped to improve this publication significantly.

APPENDIX A

KINEMATIC PROFILES

In Figure 16, we present major and minor axis kinematic profiles for the galaxies in our sample. The corresponding slit

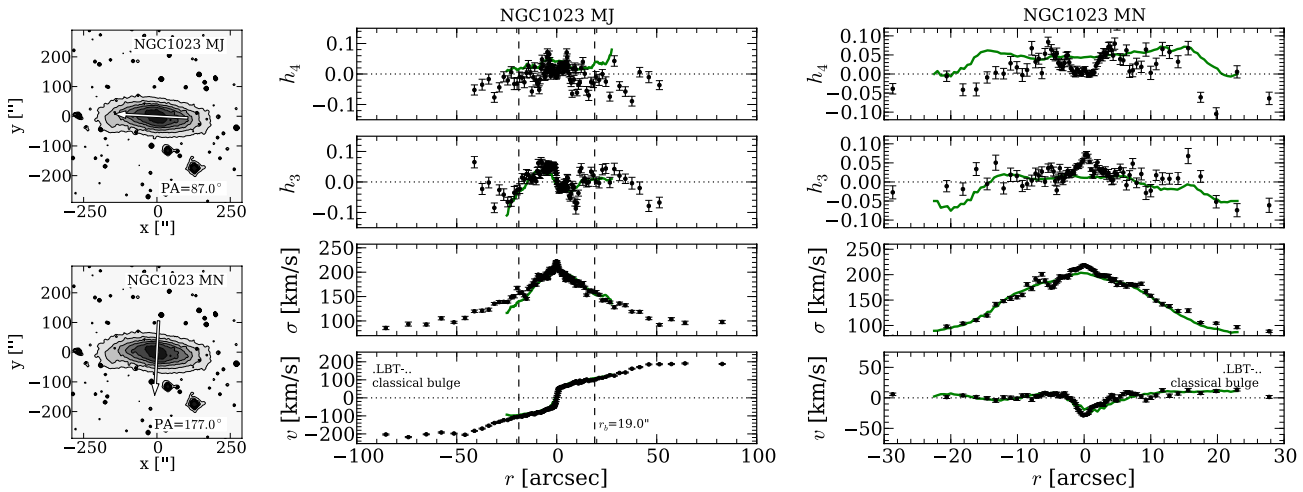

Figure 16. Major and minor axis kinematic profiles for NGC 1023. The slit position is indicated as an arrow on a Digital Sky Survey image on the left. Positive radii are east of the galaxy center. We plot from bottom to top the rotational velocity, velocity dispersion, and h_3 and h_4 moments. Vertical dashed lines indicate the bulge radius. We plot SAURON results of Emsellem et al. (2004) in green. We matched our minor axis velocities to the SAURON velocity map by allowing an offset of the slit position. A 2″ offset to the west yielded the smallest residuals between the SAURON velocities and ours.

(The complete figure set (45 images) is available in the online journal.)

position is indicated as an arrow on a Digital Sky Survey image. Positive radii are east of the galaxy center. We plot the rotational velocity, velocity dispersion, and h_3 and h_4 moments. When available we also plot data from the literature for comparison.

APPENDIX B

NOTES ON INDIVIDUAL GALAXIES

B.1. Classical Bulges

NGC 1023 .LBT-..—Clean classical morphology in *HST* F555W. The rotation curve steps rapidly from ≈+60 km s^{-1} to ≈−60 km s^{-1} in the central two arcseconds and then rises gradually to a value of ≈200 km s^{-1} at 50″. The h_3 profile shows an equally fast change within the inner ≈2″ from −0.03 to 0.03 with opposite sign. Like Emsellem et al. (2004) we see that the v/h_3 anti-correlation turns into a correlation outward of ≈10″. The velocity dispersion profile rises all the way to the center. Outside of 50″ the velocity dispersion profile flattens out at about 100 km s^{-1} which coincides with a flattening in the rotation curve. This is significantly beyond the bulge radius of ≈19″. The minor axis rotation is mostly close to zero at larger radii but becomes negative inward of 4″ (≈−25 km s^{-1} at the center). The acquisition image does not show an obvious offset of the minor axis slit but we note that due to the rapid rise of major axis rotation in the central arcseconds already a small offset of (≈0.5″) to the west suffices to explain the observed behavior. The h_3 moments become positive in the same radial range, which is expected if the velocity offset is due to actual rotation. The minor axis h_4 moments show a double peak at ±7″ with maximum values of $h_4 \approx 0.04$. The continuously centrally rising velocity dispersion of the major axis is reproduced on the minor axis.

NGC 2775 .SAR2..—The *HST* F606W image shows a very clear classical morphology, the F450W image shows very little amounts of dust in the central region. We see a depression in the velocity dispersion profile inward of 5″ in the major axis profile as well as in the minor axis profile which coincides with a steeper part in the rotation curve. Eskridge et al. (2002) describe a large, slightly elliptical bulge which contains a bright nuclear point source. The *Spitzer* MIPS 24 μm image shows a resolved nuclear source of emission which clearly stands out from a region of low emission which again in size roughly corresponds to the bulge radius. This may hint at a cold nuclear component with active star formation which dominates the kinematics. We exclude the data inward of 5″ from our analysis but note that this choice does significantly affect the position of NGC 2775 in the plane of Sérsic index versus velocity dispersion slope.

NGC 2841 .SAR3*.—The *HST* F438 image shows a weak nuclear dust spiral that is misaligned with the outer disc. The larger scale bulge morphology is smooth and shows little sign of dust and no spiral pattern. The h_3 profile is anti-correlated with the rotation curve inward of 4″ but then changes sign and becomes correlated with the velocity until about 20″. The velocity dispersion profile is centrally rising and may show a little shelf inward of ≈5″. The minor axis rotation curve shows an offset within the bulge radius.

NGC 2859 RLBR+..—Prominent outer ring galaxy. This galaxy has no close to *V*-band *HST* image available. The bulge morphology in *HST* F814W and in the acquisition images is generally smooth and classical with few weak dust lanes. Our HET long-slit data do not cover the full bulge region ($r_b = 27.6$ arcsec). Still the rotation curve starts to flatten out at our outermost data point at $r \approx 8$ arcsec. Within this region the velocity dispersion profile rises centrally from about 125 km s^{-1} at ±6 arcsec to 175 km s^{-1} in the center. The h_3 moments are clearly anti-correlated with velocity. The h_4 moments show indication of the double peak signature at $r \approx \pm 5''$. The minor axis kinematic data only reach out to 6 arcsec with little rotation along the minor axis (less than 25 km s^{-1}). The coverage of the dispersion profile in insufficient to judge whether the central rise seen along the major axis is reproduced. The minor axis h_3 and h_4 moments are somewhat noisy but do not exceed values of 0.05 and show no significant trends.

NGC 2880 .LB.-..—The bulge morphology is classical in *HST* F555W. Erwin (2004) finds indication of a weak inner disk but acknowledges that this is the weakest case in his sample. The velocity dispersion profile rises centrally with a weak non-symmetric shelf-like structure inward of ≈4″. The h_3 moments are anti-correlated with velocity within the bulge.

NGC 3031 .SAS2..—M81, interacting with the M81 group. Prominent central emission features connected to a liner-type activity prevent us from deriving the central kinematics ($r <$ ±2 arcsec) reliably. This galaxy exhibits an interesting shape of its velocity dispersion profile. The profile first rises gradually until ≈150 km s^{-1} at radius of about 25″. It then drops quickly to a minimum of about 130 km s^{-1} at 18″ and rises then again to ≈160 km s^{-1} at the center. The drop around 18″ is accompanied by a rapid change of slope of the rotational velocity which stays relatively flat outward of this radius and a strengthening of the h_3 moments. Also the otherwise vanishing h_4 moments rise to positive values (≈0.1) at $r \approx 15''$ where they form the most prominent double peak feature of our sample. The minor axis profile shows similar local minima in the dispersion profile that are accompanied by local maxima in the h_4 moments at radii of about 9″. Given the inclination of 59° this points to a flattened structure within the bulge.

NGC 3245 .LAR0*.—The *HST* F547M image reveals a nuclear dust disk while the larger scale bulge morphology is classical. This galaxy potentially hosts a lens (de Vaucouleurs et al. 1991). The rotational velocity exhibits a shelf reaching from about 3″ out to the bulge radius at 15″. The velocity dispersion profile rises steadily toward the center. The h_3 moments are anti-correlated with velocity inward of 5″. At 5″ they reach a maximum and then drop to zero toward the bulge radius. The h_4 are compatible with zero at the bulge radius ($r_b = 8.5$ arcsec) but with decreasing radius briefly drop to about −0.05 at ±5″. Finally inside of 2″ they become compatible with zero.

NGC 3521 .SXT4..—The latest Hubble type with classical bulge in our sample. In *HST* F606W the classical bulge morphology stands in strong contrast to the strong outer disk spiral structure with a sudden transition of those two morphologies at r ≈10″. The rotation curve forms a shelf at about 3″ but rises again slightly toward larger radii and starts to flatten out at 16″. The velocity dispersion reaches a local maximum of ≈115 km s^{-1} at the bulge radius ($r_b = 10.8''$) but then strongly drops with decreasing radius and reaches a local minimum of ≈100 km s^{-1} at 4″. Further inward the dispersion is centrally peaked. Outside the bulge region the dispersion shows another local maximum around 40″ which also corresponds to a slight secondary shelf on the rotational velocity. The h_3 moments are anti-correlated with velocity and form a shelf at about the same radii where the inner shelf in rotational velocity is seen. Outside the bulge, h_3 becomes rather strong (up to 0.22) and is accompanied by strong, positive h_4 moments of up to 0.15. These large moments are a consequence of the double-peak structure of the LOSVDs which has

been previously reported by Zeilinger et al. (2001) caused by a secondary kinematic component (see Section 5.7). The minor axis velocity dispersion profile does not show the strong local minima that the major axis profile shows but is similarly disturbed outside the bulge.

NGC 3898 .SAS2..—Outer disk dust spiral transitions into weak dust lanes over a smooth and classical bulge morphology in *HST* F606W. The rotation curve rises slowly out to $r \approx 10''$ and flattens at about the bulge radius of $\approx 15.7''$. The velocity dispersion profile is strongly centrally peaked and rises smoothly from ≈ 140 km s^{-1} to ≈ 220 km s^{-1} in the center. The h_3 moments are anti-correlated with velocity and reach local maximum at $r \approx 10''$, the same radius where the flattening of the rotation curve sets in.

NGC 3992 .SBT4..—This galaxy is prominently barred. While the bulge morphology generally appears classical it exhibits a few randomly distributed dust lanes in the only available optical *HST* image in F547M. With increasing radius the velocity profile reaches a first plateau at $r \approx 7''$ but outside the bulge radius of $13.2''$ it starts rising again slowly. The velocity dispersion profile is significantly depressed within the bulge region. The h_3 moments are strongly anti-correlated with velocity inward of $7''$ but become weaker further out. The h_4 moments show double peak feature around 8 arcsec.

NGC 4203 .LX.-*.—This galaxy represents a borderline case in the morphological bulge classification. The bulge has a few dust lanes in *HST* F555W superimposed on a generally smooth morphology. Fisher & Drory (2008) classify the bulge as classical. The major axis velocity profile flattens out at about the bulge radius of $14.7''$. The velocity dispersion profile shows a prominent rise from about 105 km s^{-1} at the bulge radius to 175 km s^{-1} in the center. The h_3 moments are mostly compatible with zero in the bulge region. The h_4 moments are noisy and show no significant trend within the covered region.

NGC 4260 .SBS1..—Strongly barred. The bulge morphology is generally smooth. Martini et al. (2003) acknowledge the presence of dust structures in the central region but claim that they do not imply a sense of rotation. The bulge is classified as a classical bulge by Fisher & Drory (2008). The velocity dispersion profile is somewhat irregular and S-shaped within the bulge region. The h_3 moments are small and mostly compatible with zero, The h_4 moments show a gradual drop from a central value of zero to about -0.06 at about $10''$.

NGC 4379 .L..-P*—Exhibits a very smooth and featureless, classical central morphology in *HST* F555W. The bulge radius is $8.6''$. The inset of the flattening of the rotational velocity occurs already at 8–$10''$. The velocity dispersion profile is centrally peaked, rising from ≈ 90 km s^{-1} at $10''$ to ≈ 120 km s^{-1} in the center. The h_3 moments are generally small (within the errors mostly compatible with zero) but an overall trend points to anti-correlation with velocity. The h_4 values are noisy but mostly compatible with zero.

NGC 4698 .SAS2..—*HST* F606W shows some weak dust lanes in the central region which do not, however, imply any sense of rotation. It is classified as a classical bulge by Fisher & Drory (2010). Falcón-Barroso et al. (2006) find that the stellar velocity field displays rotation perpendicular to the major axis within the central $\approx \pm 5''$. The major axis rotational velocity is very slowly rising indicative of counter-rotation. The velocity dispersion profile is mostly flat within the bulge region ($r_b = 10.7''$) with a weak central peak. In the small radial range that our data cover the h_3 and h_4 moments are mostly compatible with zero.

NGC 4772 .SAS1..—The bulge morphology is smooth and featureless in *HST* F606W, and the bulge is consequently classified as classical by Fisher & Drory (2008). The [O III] map of Falcón-Barroso et al. (2006) shows almost counter-rotation with respect to the stars in the central $\approx \pm 5''$ (see also Haynes et al. 2000). Our data virtually only cover the bulge region. The velocity dispersion profile is generally noisy with values between 100 km s^{-1} and 150 km s^{-1} but features a clear central peak. The h_3 moments are anti-correlated with velocity and reach values of up to about ± 0.07. h_4 moments scatter around values of 0.05 at all radii.

B.2. Pseudobulges

NGC 2681 PSXT0..—Possibly a triple barred system (Erwin & Sparke 1999). In *HST* F555W a dust spiral is seen, which extends all the way into the center. The rotational velocity curve shows a shelf between ≈ 2 and $\approx 12''$. The outer radius of the shelf region coincides with the bulge radius ($r_b = 13.2''$). Inward of $2''$ the rotation curve drops quickly to zero. With decreasing radius, the velocity dispersion rises from about 50 km s^{-1} to a value of ≈ 75 km s^{-1} at the bulge radius. Toward smaller radii it first stays relatively constant but then shows a step at about $5''$ and rises again inward of $2''$. The h_3 moments are anti-correlated with velocity in the region of the fast velocity rise but become correlated in the velocity shelf region. The h_4 moments show a double peak feature in the radial range of 2–$4''$.

NGC 2964 .SXR4*.—High contrast dust spiral in *HST* F606W. The bulge is small ($r_b = 3.1''$) and we do not sufficiently resolve it to include this galaxy in any of our structural plots. Here we publish the kinematic profiles. The velocity dispersion rises from values of about 40 km s^{-1} in the disk to ≈ 106 km s^{-1} at the bulge radius and exhibits a depression within the bulge. h_3 and h_4 moments scatter strongly within values of ± 0.1 which is possibly a consequence of the dust.

NGC 3166 .SXT0..—The *HST* F547M image shows strong dust features and a dust spiral which extends all the way into the center. Laurikainen et al. (2004) describe this galaxy as strongly barred. The velocity dispersion profile shows a strong depression at $\approx 4.5''$ which is accompanied by relatively strong h_3 moments of ± 0.17 and positive h_4 moments and a local maximum in the rotation curve. The minor axis shows small but significant rotation within the bulge region ($\approx \pm 10$ km s^{-1}) while the h_3 moments are largely compatible with zero. The depression of the velocity dispersion is also seen on the minor axis whilst not as strong.

NGC 3351 .SBR3..—The bulge hosts a clear spiral structure and a nuclear ring (Fisher & Drory 2010) and shows signs of active star formation. SAURON data (Dumas et al. 2007) show a drop in the gas velocity dispersion derived from Hβ and lowered [O III]/Hβ ratios in the ring indicative of star formation. The velocity dispersion profile shows a depression within the bulge region—most strongly at $r \approx 5''$ down to a value of 70 km s^{-1}—and rises again centrally to ≈ 90 km s^{-1} which is still below the values of about 100 km s^{-1} seen just inside of the bulge radius ($r_b = 12.9''$). The h_3 moments are clearly anti-correlated with velocity. The minor axis profile shows significant rotation ($v_{\rm max} \approx 50$ km s^{-1}) indicative of a slit misalignment, in fact there is a 25° difference between our major axis slit position of 165° and the Hyperleda published value of $9\overset{\circ}{.}9$.

NGC 3368 .SXT2..—Complex morphology with a number of stellar components (Erwin 2004; Nowak et al. 2010). This galaxy is possibly double-barred (Jungwiert et al. 1997). The bulge hosts a strong nuclear spiral and an inner disk (Erwin

2004) and is classified as a pseudobulge by Fisher & Drory (2010). The bulge radius is 20.4″. The complex morphology is reflected in the kinematic structure. The rotational velocity reaches a local maximum at about 7″. This is accompanied by local minimum in the velocity dispersion profile that has been rising inward until ≈13″. Inward of 7″ the dispersion rises again, but asymmetrically about the center; see Nowak et al. (2010). The local maximum in velocity and local minimum in dispersion coincide with strengthened h_3 moments. h_3 is anti-correlated with velocity inward of 15″ but correlated outside. The h_4 moments are close to zero at 13″ but become positive and reach a local maximum at about the same radii where the local maxima in velocity are observed and the drops in velocity dispersion and strengthening of h_3 moments occur. The minor axis profile shows similar depressions in velocity dispersion. The minor axis velocity profile shows a central peak of about 30 km s^{-1}. Visual inspection of the HET pre-acquisition images reveals that a minor offset of the slit position (≈1″) to the west is responsible for the peak.

NGC 3384 .LBS-*.—Contains a nuclear bar (Fisher & Drory 2010) and a rapidly rotation disk described by Busarello et al. (1996); Fisher (1997) and Emsellem et al. (2004) already find strong h_3 moments in anti-correlation with velocity. The velocity dispersion profile changes slope at 10″ and becomes more shallow toward smaller radii, but then exhibits a pronounced peak inward of 3″ that is accompanied by a dip (as seen by Fisher 1997 and Emsellem et al. 2004 as well) in the h_4 moments that become positive just outside of this region.

NGC 3627 .SXS3..—Prominently barred galaxy with wide, open arms, interacting with the Leo group. High contrast dust lanes that extend to the very center are seen in *HST* F606W and let Fisher & Drory (2008) classify this as a pseudobulge. After a fast rise the rotational velocity forms a shelf between 3″ and the bulge radius of about 11″. Toward larger radii the velocity rises again. The velocity dispersion rises inward, starting already far outside the bulge radius. At ≈4″ it flattens out and stays essentially constant. The h_3 moments are anti-correlated with velocity inside of 9″ but change sign at larger radii and become correlated with velocity. While the minor axis rotation is compatible with zero at larger radii it exhibits significant rotation inward of about 7″ that is also seen in anti-correlated h_3 moments.

NGC 3675 .SAS3..—The *HST* F606W image clearly shows a high contrast flocculent spiral that extends all the way into the center. The velocity dispersion reaches a maximum of about 110 km s^{-1} at ≈40″ and stays rather constant inside of this radius. The h_3 moments are anti-correlated with velocity within the bulge and reach maximum values of about 0.1 at the bulge radius of 8.5″.

NGC 3945 RLBT+..—Double barred (Kormendy 1979, 1982; Wozniak et al. 1995; Erwin & Sparke 1999, 2003; Erwin 2004) galaxy with prominent outer ring. Exhibits complicated kinematic structure. The rotational velocity has local minima around 18″, then rises toward smaller radii and reaches a local maximum around 8″ before it falls off to the center. The dispersion profile has very strong local minima—drops from ≈150 km s^{-1} to ≈110 km s^{-1}—at $r \approx 8''$ but then rises again toward the center. This galaxy shows exceptionally strong h_3 moments of up to ≈0.25 which are anti-correlated with velocity in the inner region but become positively correlated at about 20″. The h_4 moments are similarly strong (up to 0.2) with significant central depression. The LOSVDs do show significant low velocity shoulders at radii between $2'' < \|r\| < 10''$ which is indicative of a distinct kinematic component (see Section 5.7). The minor axis profile also shows a local depression in velocity dispersion but at $r \approx 3.5''$, the central dip in h_4 is seen as well. We measure slight rotation ($i \approx \pm 25$ km s^{-1}) along the observed position angle of $i = 64^\circ$ and a significant central offset of the velocity (≈40 km s^{-1}). The major axis velocity profile shows that a slit position offset of 1″ is sufficient to explain the central velocity peak. A visual inspection of the preacquisition image confirmed that such an offset was indeed present (about 0.6″).

NGC 4030 .SAS4..—The flocculent spiral structure—easily seen in *HST* F606W—extends all the way to the center with star-forming knots in the inner disk (Eskridge et al. 2002). Fisher & Drory (2008) classify it as pseudobulge. The major axis rotational velocity reaches ≈100 km s^{-1} at about ±10″. The velocity dispersion stays moderately flat within the bulge region and drops off outside; this was also observed by Ganda et al. (2006). The h_3 moments are clearly anti-correlated with velocity and reach values of up to 0.1 at a radius of about 7″. h_4 moments are compatible with zero at all radii that are covered by our data. The bulge is small ($r_b = 3.0''$) and we do not sufficiently resolve it to include this galaxy in any of our structural plots.

NGC 4274 RSBR2..—Double barred galaxy (Shaw et al. 1995; Erwin 2004). It is classified as pseudobulge with a Sérsic index of 1.60 ± 0.35 by (Fisher & Drory 2010). The bulge hosts a prominent nuclear spiral including strong dust lanes and a nuclear ring. The ring is seen as a fast-rotating, low-dispersion component in SAURON velocity and dispersion maps (Falcón-Barroso et al. 2006). It also appears in their ionized gas maps through increased Hβ emission and lowered [O III]/Hβ ratios which indicates star formation. The major axis rotational velocity rises quickly with increasing radius and starts flattening out at about 4″, well within the bulge radius of 11.3″. The velocity dispersion profile shows a strong depression inside the bulge with values of about 100 km s^{-1}. Outside the bulge the dispersion rises to values exceeding 130 km s^{-1}. The h_3 moments are well anti-correlated with velocity in the radial range that is covered by our data. They reach values of up to ±0.14 at about the same radius where the rotational velocity starts to flatten out. This is accompanied by peaks in the h_4 moments with values of up to 0.14.

NGC 4314 .SBT1..—Strongly barred galaxy with prominent nuclear ring. The ring appears in SAURON ionized gas maps (Falcón-Barroso et al. 2006) through lowered velocity dispersions, increased Hβ and lowered [O III]/Hβ which indicates star formation. The bulge is consequently classified as a pseudobulge by Fisher & Drory (2008). The rotational velocity starts to flatten at the bulge radius of 8.6″. The velocity dispersion profile is asymmetric but relatively flat, it varies between values of 105 km s^{-1} and 130 km s^{-1}. The S/N only allows us to derive h_3 and h_4 moments inside a radius of 6″. The h_3 moments are mostly compatible with zero, the h_4 moments rise from zero in the center to values around 0.05 at 4″.

NGC 4371 .LBR+..—Strongly barred galaxy. Erwin & Sparke (1999) find a bright stellar ring that is notable by adjusting the contrast of the *HST* F606W image carefully or through unsharp masking. While free of obvious dust or spiral structures the ring with a radius of about 5″ falls within the bulge radius which lets Fisher & Drory (2010) classify this as a pseudobulge. The major axis rotational velocity starts to flatten out at a radius of 8″—well inside the bulge radius or 22.9″—with a weak shelf around 3–8″. The velocity dispersion rises from about 105 km s^{-1} at the bulge radius to about 130 km s^{-1} at 7″.

Inside of 7″ the velocity dispersion stays relatively constant. The h_3 moments are somewhat asymmetric but generally anti-correlated with velocity within the bulge. The h_4 moments are compatible with zero in the center but rise gradually to values of about 0.05 at 10″. The minor axis velocity dispersion stays mostly constant within the covered radial range. The minor axis h_3 moments remain compatible with zero while the h_4 moments rise from zero at the center to values of about 0.05 at ±9″.

NGC 4394 RSBR3..—Strongly barred galaxy with a face-on spiral in the central $r \approx 5''$. Fisher & Drory (2008) classify it as a pseudobulge. The major axis velocity profile rises quickly to about 50 km s^{-1} at 3″. The velocity dispersion exhibits two prominent maxima around ±7″. The maxima reach values of about 105 km s^{-1} but drop quickly to about 80 km s^{-1} at 4″ and stay relatively constant toward smaller radii from there on. The h_3 moments are anti-correlated with velocity inside the bulge. The h_4 values are asymmetric and somewhat large within the bulge with values of up to 0.07 but we note that with dispersion values around 80 km s^{-1} we reach the limit of our ability to resolve those values properly.

NGC 4448 .SBR2..—Fisher & Drory (2010) note a mild spiral structure that extends into the center and classify it as a pseudobulge. The major axis rotational velocity starts to flatten out at about 5″—just inside of the bulge radius of 8.5″. Outside of 5″ the velocity profile exhibits a weak shelf. The velocity dispersion is mostly constant at a value of ≈115 km s^{-1} at all radii covered by our data. The h_3 moments are somewhat asymmetric, close to zero at positive radii but vary strongly at negative radii. The h_4 moments scatter about zero in the bulge region with a few outliers at −0.05.

NGC 4501 .SAT3..—A nuclear spiral extends all the way to the center in *HST* F606W. Fisher & Drory (2010) classify the bulge as a pseudobulge. The major axis velocity profile rises quickly from the center to the bulge radius of 6.2″ but then flattens out at the bulge radius and forms a shelf out to about 20″. The velocity dispersion rises from 75 km s^{-1} in the disk to about 150 km s^{-1} at 15″. The h_3 moments are strongly anti-correlated with velocity inside the bulge and reach values of ±0.1 at the bulge radius. h_4 moments are mostly compatible with zero at all radii. The minor axis velocity dispersion profile starts rising with decreasing radius inward of 30″ and reaches a maximum of ≈155 km s^{-1} at $r = 10''$. The minor axis velocity dispersion exhibits a central depression of about 15 km s^{-1}. The minor axis velocity, h_3 and h_4 moments are mostly compatible with zero.

NGC 4536 .SXT4..—A strong dust spiral extends into the very center. Fisher & Drory (2008) classify the bulge as pseudobulge. The bulge radius is 10.1″. The major axis rotational velocity flattens well inside bulge radius at around 2″. The velocity dispersion profile is slightly asymmetric but mostly constant within the bulge region. The h_3 moments are anti-correlated with velocity inside the bulge region and reach values of about 0.1. The h_4 profile is asymmetric. The minor axis velocities show slight asymmetric rotation (≈25 km s^{-1}). The velocity dispersion profile rises centrally but stays relatively flat within ±10″. The minor axis h_3 moments are somewhat noisy but seem to show a central depression.

NGC 4569 .SXT2..—A nuclear spiral extends all the way to the center. The bulge is classified as a pseudobulge by Fisher & Drory (2010). The major axis rotational velocity rises with increasing radius to a local maximum of about 80 km s^{-1} at ±3″. The bulge radius is $r_b = 9.6''$. The velocity then drops to about 50 km s^{-1} at the maximum radius covered by our data. The velocity dispersion rises with decreasing radius to about 100 km s^{-1} at a radius of 6″ and then drops and reaches a local minimum at around 3″, roughly coinciding with the locations of the local maxima in the velocity profile. The h_3 moments are anti-correlated with velocity inside the bulge. Their absolute values reach up to 0.15. The h_4 moments show a strong double peak feature at about 3″ and fall off to zero at the bulge radius. The minor axis profile shows rotation in the bulge region. While somewhat asymmetric, the minor axis dispersion profile does not show the same complicated structure of the major axis profile. The h_3 moments on the minor axis are mostly compatible with zero. The h_3 moments on the minor axis are mostly slightly positive with a mean value of 0.03. The h_4 moments are generally noisy but the double peak feature of the major axis is reproduced.

NGC 4736 RSAR2..—Hosts a nuclear bar (Sakamoto et al. 1999) and prominent nuclear spiral which extends all the way into the center in *HST* F555W. The bulge is classified as pseudobulge by Fisher & Drory (2010). The obtained kinematic data extend well into the disk. The rotational velocity flattens out abruptly at about the bulge radius of 14.2″ and shows a shallow negative gradient out to about 70″ where our data points start to become sparse. The velocity dispersion rises abruptly from about 75 km s^{-1} to 115 km s^{-1} at about the bulge radius. Well within the disk at radii larger than 50″ we see again a gradual increase of velocity dispersion. Inside of 2.5″ the velocity dispersion exhibits a central drop. The h_3 moments are anti-correlated with velocity but show s-shape around the center. They reach exceptionally large values of ±0.2 at the bulge radius. The h_4 moments are compatible with zero in the inner bulge but reach pronounced local maxima of values as large as 0.25 at about the bulge radius. They fall off to zero at $r \approx 35''$. These strong higher moments are a consequence of the multicomponent structure of the LOSVDs at the respective radii (see Section 5.7). The minor axis profile reflects the rich structure seen in the major axis profile. The velocity dispersion rises significantly inward of 10″. The h_3 moments are mostly compatible with zero at all radii, h_4 moments are zero inside of 10″ but rise to about 0.1 at 20″.

NGC 5055 .SAT4..—The *HST* F606W image shows that the outer disk flocculent spiral extends into the very center. Consequently this galaxy is classified as pseudobulge by Fisher & Drory (2010). The velocity dispersion profile remains flat inside the bulge radius of 18.3″. The h_3 moments are anti-correlated with velocity inside the bulge and reach absolute values of up to 0.1 at the bulge radius. The h_4 moments are compatible with zero inward of 10″. They become noisy further out but show a weak tendency toward more positive values toward the bulge radius. The minor axis velocities appear somewhat irregular but small (<20 km s^{-1}). The minor axis h_3 moments are noisy but mostly scatter close to zero. Again the h_4 moments are mostly compatible with zero inward of 10″. but show a weak increase further out but only on the east side.

NGC 5248 .SXT4..—Has a prominent nuclear spiral clearly visible in *HST* F814W. SAURON maps show the presence of a nuclear ring in Hβ and [O III] emission. A lowered [O III]/Hβ shows that the ring is star-forming. The bulge was classified as a pseudobulge by Fisher & Drory (2010). The rotational velocity starts to flatten at about 6″—well inside the bulge radius of 15.4″. The velocity profile shows a shelf between ≈10″ and ≈40″. The velocity dispersion profile is mostly flat at about 80 km s^{-1} with two small peaks at $r \approx \pm 4''$. The h_3 moments

are anti-correlated with velocity and reach values of up to ±0.1. The h_4 moments scatter around values of 0.05.

NGC 5566 .SBR2..—Shows a nuclear spiral in *HST* F606W. The surface brightness profile does not resemble a traditional bulge plus disk structure. We do not include this galaxy in any of the structural plots and publish only the kinematic profile here. The rotational velocity starts to flatten at 6″. The velocity dispersion profile rises toward the center and peaks at a value of about 150 km s^{-1}. The h_3 moments are anti-correlated with velocity and reach values of up to 0.15. The h_4 moments are small in the central arcseconds but rise to values of about 0.1 at ≈±5 arcsec.

NGC 7177 .SXR3..—A nuclear bar extends out to about $r = 10''$. The bulge is classified as a pseudobulge by Fisher & Drory (2010). The flattening of the major axis rotational velocity coincides with bulge radius of $r_b = 8.6''$. The velocity dispersion rises from about 50 km s^{-1} in the disk to values of ≈115 km s^{-1} inside the bulge but remains relatively flat inside the bulge radius. The h_3 moments are weakly anti-correlated with velocity but remain small. The h_4 moments drop to values of −0.05 at ≈±5″. The minor axis shows an asymmetric velocity profile with values of up to ±25 km s^{-1}. The minor axis velocity dispersion again rises from about 50 km s^{-1} in the disk to values of about 115 km s^{-1} at 2.5″ and remains flat inside. The h_3 moments are anti-correlated with velocity. The h_4 moments are noisy and scatter around zero.

NGC 7743 RLBS+..—The central region exhibits some weak dust lanes overlaid on a generally (Martini et al. 2003) smooth light distribution. The bulge is classified as classical bulge by Fisher & Drory (2008). The amplitude of the rotation is small at about ±25 km s^{-1} due to the low inclination. We find rotation of similar value along the minor axis slit due to a misplacement of the slit (166° rather than 10°). The velocity dispersion is flat for both position angles and takes values of about 80 km s^{-1}. Both, major axis and minor axis h_3 moments are anti-correlated with velocity and become compatible with zero at the bulge radius ($r_b = 5.6''$). The h_4 moments are very noisy, probably due to the low velocity dispersion of this object.

B.3. Bulges without Classification

NGC 2460 .SAS1..—Mixed-type morphology in *HST* F606W with a weak asymmetric dust structure in the bulge region that is overlaid on an otherwise smooth light distribution. We label this bulge as unclassified. The decomposition gave a value of 3.5 ± 0.32 for the Sérsic index and 6.6″ for the bulge radius. Within this region the velocity dispersion profile is flat and h_3 and h_4 moments scatter around zero.

NGC 3593 .SAS0*.—Peculiar bulge structure with prominent spiral visible even in NIC F160W. The bulge is classified as a pseudobulge by Fisher & Drory (2010). We label it as non-classified because its high inclination inhibits an unperturbed view into the bulge region. This is the only example in our sample where counter-rotation is seen in the velocity profile as an actual change of the sign of the velocity with respect to the systemic velocity (this was found also by Bertola et al. 1996). The counter-rotation within the bulge radius is reflected in the anti-correlated h_3 moments. The velocity dispersion drops dramatically from ≈115 km s^{-1} at the bulge radius to ≈60 km s^{-1} in the center.

NGC 3953 .SBR4..—Fisher & Drory (2010) classify this bulge as pseudobulge but acknowledge that there is no optical *HST* image available. Here we label it as nonclassified. The rotational velocity profile first reaches a weak local maximum at $r \approx 2.5''$ before it starts rising again outside of 8″. The disk velocity dispersion rises centrally from values of ≈50 km s^{-1} at ±30″ to ≈130 km s^{-1} at ≈8″. Inside of a radius of 6″ it then falls toward a central value of ≈110 km s^{-1}. The fast central increase of velocity is accompanied by strong anti-correlated h_3 moments with values of up to ±0.1 at $r \approx 6''$; they become correlated with velocity outside of 8″. The h_4 moments are generally noisy in the bulge region and scatter between zero and 0.05.

NGC 4826 RSAT2..—Also named the "black eye" galaxy. An extreme dust spiral in the central 50″ stands in strong contrast to a virtually dust free outer disk. The central dust content leads to a classification as pseudobulge in Fisher & Drory (2008). The major axis kinematic profile is rich in structure. The rotational velocity rises quickly from the center to a value of ≈50 km s^{-1} at $r = 4''$. It then forms a shallow trough around 8″ and then rises again—more slowly—out to 50″ where it finally flattens out. The velocity dispersion in the disk is ≈45 km s^{-1}, it shows a distinct central increase inward of 50″. The dispersion reaches values of up to 110 km s^{-1} inside of the bulge radius ($r_b = 25.4''$). From there on it stays relatively constant with decreasing radius except for a mild depression down to 90 km s^{-1} in the central few arcseconds. The h_3 moments are strongly anti-correlated with velocity for $r < 9''$ and reach absolute values of up to 0.15. The h_4 moments show two peaks at about ±3″. We find weak rotation along the minor axis (≈±10 km s^{-1}). The central increase in velocity dispersion is also seen along the minor axis, the increase sets in at a radius of about 25″. This is much closer to the center than in the case of the major axis and points to a flattened structure. For the photometry we obtain a mean bulge ellipticity of 0.23. The radial difference of the dispersion increase along the major and the minor axis would point to an ellipticity of about 0.45. The center of the velocity dispersion profile is asymmetric which may be a consequence of the strong dust. The minor axis h_3 and h_4 moments are compatible with zero. The fact that the final flattening of the rotational velocity and the inset of the dispersion increase at 50″ coincides with the sudden appearance of the strong dust structure is intriguing and lets one suspect that the actual bulge radius fall closer to 50″. The much smaller bulge radius from the decomposition may be a consequence of the strong dust content in the central regions (see also discussion in Section 5.4).

NGC 7217 RSAR2..—Fisher & Drory (2010) point out a sudden break in morphology at a radius of about 8″ where the outer spiral transitions onto a relatively smooth morphology with little dust. They consequently label this bulge as classical. However, we determine a bulge radius of 11.2″ where there is already a pronounced spiral pattern visible. We label this galaxy as nonclassified. The rotational velocity profile starts to flatten out at about the bulge radius. The major axis dispersion profile is asymmetric with higher values on the east side of the center. Within the central ±2″ the velocity dispersion shows a mild depression of about 20 km s^{-1}. The h_3 moments are well anti-correlated with velocity. The h_4 moments scatter around values of 0.05. We observe mild rotation on the minor axis (of the order of ±10 km s^{-1}) indicative of a slight slit misalignment. The minor axis velocity dispersion is symmetric and rises toward the center from values of about 100 km s^{-1} at radii of ±20″ to 145 km s^{-1} at 2″. Within the central arcseconds the mild depression which is seen on the major axis is reproduced on the minor axis. The minor axis h_3 moments mostly scatter around zero while h_4 moments fall closer to 0.05 with a few relatively large outliers at radii around 6–10″. Merrifield &

Kuijken (1994) found the 20%-30% of the light is captured in a counter-rotating component. We confirm this and present a kinematic decomposition in Section 5.7.

NGC 7331 .SAS3..—The *HST* F555W image shows several dust lanes in the bulge region. However these do not imply any sense of rotation and seem to be overlaid on a generally smooth light distribution. Fisher & Drory (2008) admit that the high inclination leaves the classification as classical bulge questionable. Here we label it as nonclassified. The rotational velocity profile is already flattened at the bulge radius of $r_b = 26''$. The velocity dispersion rises from about 75 km s^{-1} in the disk to 125 km s^{-1} in the center. The dispersion profile has two steps or shoulders at $\approx\pm 20''$. The h_3 moments are generally anti-correlated with velocity and reach a local maximum of about ± 0.15 at $r = 15''$. Also the h_4 moments reach local maxima with values of up to 0.15 in the same radial range. These large moments are a consequence of the double-peak structure of the LOSVDs caused by a counter-rotating kinematic component discovered by Prada et al. (1996; see Section 5.7).

REFERENCES

Athanassoula, E. 2005, MNRAS, 358, 1477
Bender, R. 1990, A&A, 229, 441
Bender, R., & Moellenhoff, C. 1987, A&A, 177, 71
Bender, R., Saglia, R. P., & Gerhard, O. E. 1994, MNRAS, 269, 785
Bertola, F., Cinzano, P., Corsini, E. M., et al. 1996, ApJ, 458, L67
Bertola, F., Cinzano, P., Corsini, E. M., Rix, H.-W., & Zeilinger, W. W. 1995, ApJ, 448, L13
Bertola, F., & Corsini, E. M. 1999, in IAU Symp. 186, Galaxy Interactions at Low and High Redshift, ed. J. E. Barnes & D. B. Sanders (Cambridge: Cambridge Univ. Press), 149
Bertola, F., Corsini, E. M., Vega Beltrán, J. C., et al. 1999, ApJ, 519, L127
Bettoni, D., & Galletta, G. 1997, A&AS, 124, 61
Binney, J. 2005, MNRAS, 363, 937
Binney, J., & Tremaine, S. 1987, Galactic Dynamics (Princeton Series in Astrophysics; Princeton, NJ: Princeton Univ. Press)
Blakeslee, J. P., Jordán, A., Mei, S., et al. 2009, ApJ, 694, 556
Brault, J. W., & White, O. R. 1971, A&A, 13, 169
Braun, R., Walterbos, R. A. M., & Kennicutt, R. C., Jr. 1992, Nature, 360, 442
Braun, R., Walterbos, R. A. M., Kennicutt, R. C., Jr., & Tacconi, L. J. 1994, ApJ, 420, 558
Bureau, M., & Athanassoula, E. 2005, ApJ, 626, 159
Bureau, M., & Freeman, K. C. 1999, AJ, 118, 126
Busarello, G., Capaccioli, M., D'Onofrio, M., et al. 1996, A&A, 314, 32
Caon, N., Capaccioli, M., & D'Onofrio, M. 1993, MNRAS, 265, 1013
Cappellari, M., & Emsellem, E. 2004, PASP, 116, 138
Carollo, C. M., Stiavelli, M., de Zeeuw, P. T., & Mack, J. 1997, AJ, 114, 2366
Chung, A., & Bureau, M. 2004, AJ, 127, 3192
Ciotti, L. 1991, A&A, 249, 99
Combes, F., Debbasch, F., Friedli, D., & Pfenniger, D. 1990, A&A, 233, 82
Comerón, S., Knapen, J. H., Beckman, J. E., et al. 2010, MNRAS, 402, 2462
Corsini, E. M., Pizzella, A., Sarzi, M., et al. 1999, A&A, 342, 671
de Jong, R. S., & van der Kruit, P. C. 1994, A&AS, 106, 451
de Lorenzo-Cáceres, A., Falcón-Barroso, J., Vazdekis, A., & Martínez-Valpuesta, I. 2008, ApJ, 684, L83
de Vaucouleurs, G., de Vaucouleurs, A., Corwin, H. G., Jr., et al. 1991, Third Reference Catalogue of Bright Galaxies (Berlin: Springer)
Debattista, V. P., Carollo, C. M., Mayer, L., & Moore, B. 2005, ApJ, 628, 678
Dumas, G., Mundell, C. G., Emsellem, E., & Nagar, N. M. 2007, MNRAS, 379, 1249
Ekholm, T., Lanoix, P., Teerikorpi, P., Fouqué, P., & Paturel, G. 2000, A&A, 355, 835
Eliche-Moral, M. C., Balcells, M., Aguerri, J. A. L., & González-García, A. C. 2006, A&A, 457, 91
Eliche-Moral, M. C., González-García, A. C., Balcells, M., et al. 2011, A&A, 533, A104
Emsellem, E., Cappellari, M., Peletier, R. F., et al. 2004, MNRAS, 352, 721
Erwin, P. 2004, A&A, 415, 941
Erwin, P., & Sparke, L. S. 1999, ApJ, 521, L37
Erwin, P., & Sparke, L. S. 2003, ApJS, 146, 299
Eskridge, P. B., Frogel, J. A., Pogge, R. W., et al. 2002, ApJS, 143, 73
Faber, S. M., & Jackson, R. E. 1976, ApJ, 204, 668
Fabricius, M. H., Barnes, S., Bender, R., et al. 2008, Proc. SPIE, 7014, 234
Falcón-Barroso, J., Bacon, R., Bureau, M., et al. 2006, MNRAS, 369, 529
Falcón-Barroso, J., Balcells, M., Peletier, R. F., & Vazdekis, A. 2003, A&A, 405, 455
Falcón-Barroso, J., Peletier, R. F., Emsellem, E., et al. 2004, MNRAS, 350, 35
Fisher, D. 1997, AJ, 113, 950
Fisher, D. B. 2006, ApJ, 642, L17
Fisher, D. B., & Drory, N. 2008, AJ, 136, 773
Fisher, D. B., & Drory, N. 2010, ApJ, 716, 942
Fisher, D. B., & Drory, N. 2011, ApJ, 733, L47
Fontanot, F., De Lucia, G., Wilman, D., & Monaco, P. 2011, MNRAS, 416, 409
Gadotti, D. A., & de Souza, R. E. 2005, ApJ, 629, 797
Gadotti, D. A., & dos Anjos, S. 2001, AJ, 122, 1298
Ganda, K., Falcón-Barroso, J., Peletier, R. F., et al. 2006, MNRAS, 367, 46
Gebhardt, K., Richstone, D., Kormendy, J., et al. 2000, AJ, 119, 1157
Gerhard, O. E. 1993, MNRAS, 265, 213
Governato, F., Brook, C. B., Brooks, A. M., et al. 2009, MNRAS, 398, 312
Graham, A., & Colless, M. 1997, MNRAS, 287, 221
Hastings, W. K. 1970, Biometrika, 57, 97
Haynes, M. P., Jore, K. P., Barrett, E. A., Broeils, A. H., & Murray, B. M. 2000, AJ, 120, 703
Héraudeau, P., & Simien, F. 1998, A&AS, 133, 317
Héraudeau, P., Simien, F., Maubon, G., & Prugniel, P. 1999, A&AS, 136, 509
Hill, G. J., Nicklas, H. E., MacQueen, P. J., et al. 1998, Proc. SPIE, 3355, 433
Hopkins, P. F., Cox, T. J., Younger, J. D., & Hernquist, L. 2009, ApJ, 691, 1168
Hopkins, P. F., Hernquist, L., Cox, T. J., Younger, J. D., & Besla, G. 2008, ApJ, 688, 757
Illingworth, G. 1977, ApJ, 218, L43
Jarrett, T. H., Chester, T., Cutri, R., Schneider, S. E., & Huchra, J. P. 2003, AJ, 125, 525
Jensen, J. B., Tonry, J. L., Barris, B. J., et al. 2003, ApJ, 583, 712
Jungwiert, B., Combes, F., & Axon, D. J. 1997, A&AS, 125, 479
Knapen, J. H., de Jong, R. S., Stedman, S., & Bramich, D. M. 2003, MNRAS, 344, 527
Kormendy, J. 1979, ApJ, 227, 714
Kormendy, J. 1982, ApJ, 257, 75
Kormendy, J. 1993, in IAU Symp. 153, Galactic Bulges, ed. H. Dejonghe & H. J. Habing (Cambridge: Cambridge Univ. Press), 209
Kormendy, J., & Barentine, J. C. 2010, ApJ, 715, L176
Kormendy, J., Drory, N., Bender, R., & Cornell, M. E. 2010, ApJ, 723, 54
Kormendy, J., & Fisher, D. B. 2008, in ASP Conf. Ser. 396, Formation and Evolution of Galaxy Disks, ed. J. G. Funes & E. M. Corsini (San Francisco, CA: ASP), 297
Kormendy, J., Fisher, D. B., Cornell, M. E., & Bender, R. 2009, ApJS, 182, 216
Kormendy, J., & Illingworth, G. 1982, ApJ, 256, 460
Kormendy, J., & Kennicutt, R. C., Jr. 2004, ARA&A, 42, 603
Laurikainen, E., Salo, H., Buta, R., & Vasylyev, S. 2004, MNRAS, 355, 1251
Martini, P., Regan, M. W., Mulchaey, J. S., & Pogge, R. W. 2003, ApJS, 146, 353
Mehlert, D., Saglia, R. P., Bender, R., & Wegner, G. 2000, A&AS, 141, 449
Méndez-Abreu, J., Corsini, E. M., Debattista, V. P., et al. 2008, ApJ, 679, L73
Merrifield, M. R., & Kuijken, K. 1994, ApJ, 432, 575
Möllenhoff, C., & Heidt, J. 2001, A&A, 368, 16
Nowak, N., Thomas, J., Erwin, P., et al. 2010, MNRAS, 403, 646
Paturel, G., Petit, C., Prugniel, P., et al. 2003, A&A, 412, 45
Pignatelli, E., Corsini, E. M., Vega Beltrán, J. C., et al. 2001, MNRAS, 323, 188
Pizzella, A., Corsini, E. M., Vega Beltrán, J. C., & Bertola, F. 2004, A&A, 424, 447
Prada, F., Gutierrez, C. M., Peletier, R. F., & McKeith, C. D. 1996, ApJ, 463, L9
Press, W. H. 2002, Numerical Recipes in C++: the Art of Scientific Computing (Cambridge: Cambridge Univ. Press)
Press, W. H., Teukolsky, S. A., Vetterling, W. T., & Flannery, B. P. 2007, Numerical Recipes: The Art of Scientific Computing (3rd ed.; Cambridge: Cambridge Univ. Press)
Quinn, P. J., Hernquist, L., & Fullagar, D. P. 1993, ApJ, 403, 74
Ramsey, L. W., Adams, M. T., Barnes, T. G., et al. 1998, Proc. SPIE, 3352, 34
Rauscher, B. J. 1995, AJ, 109, 1608
Riess, A. G., Macri, L., Casertano, S., et al. 2009, ApJ, 699, 539
Saglia, R. P., Fabricius, M., Bender, R., et al. 2010, A&A, 509, A61
Saha, A., Thim, F., Tammann, G. A., Reindl, B., & Sandage, A. 2006, ApJS, 165, 108
Saha, K., Tseng, Y., & Taam, R. E. 2010, ApJ, 721, 1878
Sakamoto, K., Okumura, S. K., Ishizuki, S., & Scoville, N. Z. 1999, ApJS, 124, 403
Salpeter, E. E. 1955, ApJ, 121, 161

Sarzi, M., Falcón-Barroso, J., Davies, R. L., et al. 2006, MNRAS, 366, 1151
Scorza, C., & Bender, R. 1995, A&A, 293, 20
Sellwood, J. A., & Wilkinson, A. 1993, Rep. Prog. Phys., 56, 173
Sérsic, J. L. 1968, Atlas de Galaxias Australes (Cordoba: Observatorio Astronomico)
Shaw, M., Axon, D., Probst, R., & Gatley, I. 1995, MNRAS, 274, 369
Simien, F., & Prugniel, P. 1998, A&AS, 131, 287
Simien, F., & Prugniel, P. 2002, A&A, 384, 371
Simkin, S. M. 1974, A&A, 31, 129
Skrutskie, M. F., Cutri, R. M., Stiening, R., et al. 2006, AJ, 131, 1163
Smirnov, N. V. 1939, Bulletin of Mathematics, Univ of Moscow, 2, 3
Springob, C. M., Masters, K. L., Haynes, M. P., Giovanelli, R., & Marinoni, C. 2009, ApJS, 182, 474
Stewart, K. R., Bullock, J. S., Wechsler, R. H., & Maller, A. H. 2009, ApJ, 702, 307
Stewart, K. R., Bullock, J. S., Wechsler, R. H., Maller, A. H., & Zentner, A. R. 2008, ApJ, 683, 597
Storchi-Bergmann, T., Dors, O. L., Jr., Riffel, R. A., et al. 2007, ApJ, 670, 959
Tonry, J. L., Dressler, A., Blakeslee, J. P., et al. 2001, ApJ, 546, 681
Tully, R. B. 1994, VizieR Online Data Catalog, 7145, 0
Tully, R. B., Rizzi, L., Shaya, E. J., et al. 2009, AJ, 138, 323
Tully, R. B., Verheijen, M. A. W., Pierce, M. J., Huang, J.-S., & Wainscoat, R. J. 1996, AJ, 112, 2471
van Albada, T. S. 1982, MNRAS, 201, 939
van der Marel, R. P., & Franx, M. 1993, ApJ, 407, 525
Vazdekis, A. 1999, ApJ, 513, 224
Vega Beltrán, J. C., Pizzella, A., Corsini, E. M., et al. 2001, A&A, 374, 394
White, S. D. M., & Frenk, C. S. 1991, ApJ, 379, 52
White, S. D. M., & Rees, M. J. 1978, MNRAS, 183, 341
Worthey, G., Faber, S. M., Gonzalez, J. J., & Burstein, D. 1994, ApJS, 94, 687
Wozniak, H., Friedli, D., Martinet, L., Martin, P., & Bratschi, P. 1995, A&AS, 111, 115
Zeilinger, W. W., Vega Beltrán, J. C., Rozas, M., et al. 2001, Ap&SS, 276, 643